FINNISH METEOROLOGICAL INSTITUTE
CONTRIBUTIONS

No. 45

MESO-SCALE AURORAL PHYSICS FROM GROUND-BASED OBSERVATIONS

Noora Partamies

Department of Physical Sciences
Faculty of Science
University of Helsinki
Helsinki, Finland

Dissertation for the degree of Doctor of Philosophy to be presented with the permission of the Faculty of Science of the University of Helsinki for public critisism in Small Auditorium E204 at Physicum in Kumpula Campus on 9$^{\text{th}}$ October, 2004, at 10 a.m.

Finnish Meteorological Institute
Helsinki, 2004

ISBN 951-697-597-6 (paperback)
ISBN 952-10-2011-3 (pdf)
ISSN 0782-6117

Yliopistopaino
Helsinki, 2004

FINNISH METEOROLOGICAL INSTITUTE

Published by Finnish Meteorological Institute
P.O. Box 503
FIN-00101 Helsinki, Finland

Series title, number and report code of publication
Contributions 45, FMI-CONT-45

Date
September 2004

Authors
Noora Partamies

Name of project

Commissioned by

Title
Meso-scale auroral physics from ground-based observations

Abstract

This thesis studies the physics of meso-scale (10-1000km) auroral structures by using advanced data analysis tools developed for ground-based observations. The work especially concentrates on the appearance (size and winding direction) of auroral spiral forms. The introductory part provides the background in auroral physics, instrumentation and measurements, and the methods and models used in the following five publications.

The work utilises extensively images from the digital all-sky cameras of the MIRACLE network operating in Fennoscandia and on Svalbard. For the first time, the average characteristics of auroral spirals are determined from a vast number of all-sky images. The statistical study shows that spirals are observed during post-midnight hours and under magnetically quiet conditions more frequently than the previous satellite observations suggest. A well-known mathematical spiral model is derived in a more general form to confirm the observed winding directions on both hemispheres and to investigate in more detail the factors affecting the spiral winding. An event study shows how a complete picture of the ionospheric electrodynamics (behaviour of the ionospheric electric fields and currents) can be built around a sequence of auroral images when a large enough set of supplementary observations from other ground-based instrumentation is available. Finally, ground-based and satellite observations of auroral arcs are compared in order to test an inversion method, which converts the digital brightness of all-sky camera images into a precipitating electron energy flux, number flux and field-aligned current. With the new inversion method, energy flux values can be obtained very accurately, with relative errors of 10% at its best. However, further development is needed before all-sky camera data alone can be used to obtain numerical estimates of number fluxes or currents of the aurora.

Publishing unit
Finnish Meteorological Institute, Space Research Unit

Classification (UDC)
52, 551.510.535

Keywords
space plasma physics, ionosphere, aurora

ISSN and series title
0782-6117 Finnish Meteorological Institute Contributions

ISBN
951-697-597-6 (paperback), 952-10-2011-3 (pdf)

Language
English

Pages
122

Price

Sold by
Finnish Meteorological Institute / Library
P.O. Box 503, FIN-00101 Helsinki
Finland

Note

ILMATIETEEN LAITOS

Julkaisun sarja, numero ja raporttikoodi

Julkaisija Ilmatieteen laitos
PL 503, 00101 Helsinki

Contributions 45, FMI-CONT-45

Julkaisuaika
Syyskuu 2004

Tekijä(t)
Noora Partamies

Projektin nimi

Toimeksiantaja

Nimeke
Keskisuurten revontulimuotojen fysiikkaa maanpintamittausten avulla

Tiivistelmä

Tässä väitöskirjassa tutkitaan keskisuurten (10-1000km) revontulimuotojen fysiikkaa soveltamalla erilaisia analyysimenetelmiä maanpintamittausaineistoon. Erityisen kiinnostuksen kohteena ovat revontulien spiraalimuodot ja niiden tyypilliset piirteet kuten koko ja kiertymissuunta. Johdanto-osassa käsitellään revontulitutkimuksen taustaa, siinä käytettäviä mittalaitteita ja tehtyjä havaintoja sekä loppuosan viidessä artikkelissa julkaistuja menetelmiä ja malleja.

Väitöskirjatyö hyödyntää tehokkaasti Fennoskandiassa ja Huippuvuorilla sijaitsevien MIRACLE-instrumenttiverkon revontulikameroiden ottamia kuvia. Revontulispiraalien tyypilliset ominaisuudet määriteltiin ensimmäistä kertaa kattavan revontulikuvaston perusteella. Tässä tilastollisessa tarkastelussa kävi ilmi, että spiraaleja havaitaan ennen magneettista keskiyötä ja magneettisesti rauhallisena aikana enemmän kuin aiemmat satelliittihavainnot osoittavat. Spiraalien kehitystä kuvaavaa matemaattista mallia yleistettiin ja sen huomattiin ennustavan spiraalien kiertymissuunta oikein kummallakin pallonpuoliskolla. Mallin avulla selvitettiin myös yksityiskohtaisesti, miten ja mitkä tekijät vaikuttavat spiraalirakenteen kehitykseen. Yksittäisen revontulijakson elektrodynamiikkaa (ionosfäärin sähkökenttien ja -virtojen muutoksia) tutkittiin yhdistämällä laajalti muiden maanpintamittalaitteiden havaintoja revontulikuvissa näkyviin tapahtumiin. Lopuksi vertailtiin revontulikaarien satelliitti- ja maanpintahavaintoja. Vertailujen avulla testattiin revontulikamerakuville kehitettyä inversiomenetelmää, joka muuntaa kuvan kirkkauden elektronien kokonaisenergiavuoksi. Inversiomenetelmä voi parhaimmillaan antaa energiavuot jopa noin 10%:n tarkkuudella, mutta jatkokehittelyä tarvitaan vielä, ennen kuin pelkän revontulikuvan perusteella voidaan luotettavasti arvioida revontuliin liittyvää hiukkasvuota tai sähkövirtaa.

Julkaisijayksikkö
Avaruus- ja yläilmakehän tutkimus

Luokitus (UDK)
52, 551510.535

Asiasanat
Avaruusplasmafysiikka, ionosfääri, revontulet

ISSN ja avainnimike
0782-6117 Finnish Meteorological Institute Contributions

ISBN
951-697-597-6 (paperback), 952-10-2011-3 (pdf)

Kieli
Englanti

Sivumäärä
122

Hinta

Myynti
Ilmatieteen laitos / Kirjasto
PL 503, 00101 Helsinki

Lisatietoja

PREFACE

This thesis work has been performed at the Geophysical Research (GEO, recently changed to AVA) of the Finnish Meteorological Institute (FMI). It has been funded by the Finnish Graduate School in Astronomy and Space Physics during the first four years, and by the Academy of Finland during the last year. Additional financial support has been obtained from Pauli and Paavo Talka Foundation, Magnus Ehrnrooth Foundation, Vilho, Yrjö ja Kalle Väisälä Fund, Finnish Konkordia Fund and Sohlberg Delegation. I wish to thank these institutions for all the conference travels they made possible.

My special thanks go to my supervisor Dr. Kirsti Kauristie for her continuous encouragement, professional help with any little detail and patience in going back to the basics whenever needed. I also want to acknowledge Prof. Tuija Pulkkinen, the head of GEO, Prof. Risto Pellinen, the former head of GEO, Dr. Ari Viljanen, the head of the Space Research group and Dr. Risto Pirjola, the former head of the Space Physics group for making the working conditions pleasant in practice, not only on paper. I would like to thank Dr. Pekka Janhunen whose support was invaluable during my excursion to the inversion method. I also wish to thank all the GEO people for an inspiring atmosphere every day, and the Geodynamo members for making it rock. It has been fun to work.

I extend my gratitude to Dr. Mervyn Freeman for hosting me at the British Antarctic Survey and being a wonderful co-author. I would like to thank Dr. Fred Sigernes at the University Centre on Svalbard for organising my Marie Curie training, which turned out to be an unforgettable experience. I would also like to thank Dr. Eric Donovan and his Space Physics group for providing me excellent working conditions at the University of Calgary during the past two winters, and I am indebted to ”my Canadian family” Cindy and Darrell Everett for hilarious company and daily discussions beyond the space science.

I want to thank Dr. Reijo Rasinkangas at the University of Oulu for the on-line space physics textbook (http://www.oulu.fi/ spaceweb/textbook/), which is a wonderful source of definitions, basic concepts and references, especially when working abroad. I am sincerely grateful to Dr. Betty Lanchester from the University of Southampton and Dr. Anita Aikio from the University of Oulu for reviewing my thesis. Their work was very careful and their comments hugely helpful.

Although EISCAT has not been much of my topic, I have been lucky to join the Finnish EISCAT campaigns, learnt many things, had fun and got a lot of work done in the control room of the EISCAT Svalbard radar. So, I want to thank the Finnish campaign team and the ESR staff for guidance and company, even at 4 a.m.

I further thank my cousin Kirsi Partamies for helping me to produce understandable English. The fact that keeps space scientist's feet on the ground instead of the upper atmosphere is the contact to the real world. So finally, I want to warmly thank my family and friends for their continuous support and staying in touch.

Helsinki, August 2004

Noora Partamies

CONTENTS

LIST OF ACRONYMS 7

NOTATION AND SYMBOLS 8

LIST OF PUBLICATIONS 10

1 INTRODUCTION 11
1.1 AURORA AND SPACE PLASMA PHYSICS 11
1.2 FROM THE SUN TO THE EARTH 11
1.3 MAGNETOSPHERE 13
1.4 IONOSPHERIC CONVECTION AND CURRENTS 14
1.4.1 Structure of the ionosphere 14
1.4.2 Convection 15
1.4.3 Currents 16
1.5 AURORAL LIGHT 17

2 INSTRUMENTATION 19
2.1 MIRACLE INSTRUMENT NETWORK 19
2.1.1 Overview 19
2.1.2 All-sky cameras 20
2.1.3 Magnetometers 21
2.1.4 STARE 21
2.2 OTHER INSTRUMENTS 23
2.2.1 EISCAT radars 23
2.2.2 Satellites 24

3 OBSERVATIONS OF DIFFERENT AURORAL STRUCTURES 25
3.1 AURORAL ARCS 25
3.2 ARC DISTORTIONS: FOLDS, SPIRALS, CURLS 26

4 AURORAL ACTIVITY 29
4.1 SUBSTORM AND ITS SIGNATURES FROM THE GROUND 29
4.2 SMALL SUBSTORMS OR PSEUDO-BREAKUPS? 31

5 MODELS AND METHODS 36
5.1 SPIRAL MODEL BY HALLINAN 36
5.2 ASCINV: AN INVERSION METHOD FOR ASC IMAGES 38

5.3 OTHER METHODS 44
5.3.1 Spectrum: An inversion method for EISCAT data 44
5.3.2 Method of Characteristics 45

SUMMARY OF THE PUBLICATIONS 49

REFERENCES 51

PUBLICATIONS I–V 59

LIST OF ACRONYMS

ABK	All-sky camera station in Abisko, Sweden
ACE	Advanced Composition Explorer satellite in the solar wind
ASC	All-Sky Camera
ASCinv	Inversion method for ASC images
ASI	All-Sky Imager
AU	Astronomical Unit
CANOPUS	Canadian Auroral Network for the Open Program Unified Study
CCD	Charge Coupled Device
DMSP	Defense Meteorological Satellite Program, low altitude satellites
EISCAT	European Incoherent SCATter radar
FAC	Field-Aligned Current
FMI	Finnish Meteorological Institute
FMI/GEO	Finnish Meteorological Institute, GEOphysical research
FOV	Field-Of-View
HD	Harang Discontinuity
IMAGE	International Monitor for Auroral Geomagnetic Effects (magnetometer network)
IMF	Interplanetary Magnetic Field
KIL	All-sky camera station in Kilpisjärvi, Finland
LANL	Los Alamos National Laboratory, satellites at the geosynchronous orbit
LOS	Line-Of-Sight
MIRACLE	Magnetometers — Ionospheric Radars — All-sky Cameras Large Experiment
MUO	All-sky camera station in Muonio
NASA	National Aeronautics and Space Administration
R1 / R2	Region 1 and Region 2 currents
STARE	Scandinavian Twin Auroral Radar Experiment
SCW	Substorm Current Wedge
THEMIS	Time History of Events and Macroscale Interactions during Substorms
UHF	Ultra High Frequency (500–1000 MHz)
UT	Universal Time
UVI	UltraViolet Imager
VHF	Very High Frequency (50–300 MHz)
WTS	Westward Travelling Surge

NOTATION AND SYMBOLS

Symbol	Explanation	Chapter: Context
$\mathbf{A}$	Theory matrix	CH 5: *ASCinv*
$\mathbf{B}$	Magnetic field of the Earth	CH 1: *Ionospheric currents*
$\mathbf{B_0}$	Background magnetic field	CH 5: *Spiral model*
$\mathbf{B_1}$	Perturbation magnetic field due to an enhancement in FAC	CH 5: *Spiral model*
$\mathbf{B_{Ion,h}}$	Horizontal part of the external magnetic field	CH 5: *Method of Characteristics*
$\mathbf{E}$	Electric field	CH 1: *Ionospheric currents*
E	Energy of the precipitating electron	CH 5: *ASCinv*
$\mathbf{E_M}$	Measured ionospheric electric field	CH 5: *Method of Characteristics*
$\mathbf{E}_{PC}$	Polar cap electric field	CH 1: *Ionospheric currents*
F	Electron differential number flux	CH 5: *ASCinv*
$\mathbf{G}$	Geometry matrix	CH 5: *ASCinv*
$\mathbf{J}$	Horizontal height-integrated current density	CH 5: *Method of Characteristics*
$\mathbf{J_{df}}$	Divergence-free part of ionospheric current density	CH 5: *Method of Characteristics*
$\mathbf{P}$	Physics matrix	CH 5: *ASCinv*
R	Electron range according to Rees [1963, 1989]	CH 5: *ASCinv*
R_E	Earth radius, 6371 km	CH 1: *Solar wind-magnetosphere interaction*
R_S	Electron range according to Sergienko and Ivanov [1993]	CH 5: *ASCinv*
V_{428}	Excitation efficiency of blue photons by Rees [1963, 1989]	CH 5: *ASCinv*
V_{S428}	Excitation efficiency of blue photons by Sergienko and Ivanov [1993]	CH 5: *ASCinv*
$\mathbf{W}$	A vector related to the measured electric field	CH 5: *Method of Characteristics*
a	Half-width of an auroral arc	CH 5: *Spiral model*
e_{g2b}	Green-to-blue emission rate ratio	CH 5: *ASCinv*
e_{r2b}	Red-to-blue emission rate ratio	CH 5: *ASCinv*
$\mathbf{j}$	Field-aligned current density	CH 1: *Ionospheric currents*
k	Wave number	CH 5: *Spiral model*
$\mathbf{m}$	Measurement vector containing ASC images	CH 5: *ASCinv*
n	Neutral atmospheric density	CH 5: *ASCinv*
n_e	Number density of charged particles	CH 5: *Spectrum*
p	Thermal pressure	CH 5: *Spiral model*
q	Electron charge, $1.602{\cdot}10^{-19}$C	CH 5: *Spectrum*
$\mathbf{u}$	Vector of unknowns	CH 5: *ASCinv*

$\mathbf{v}$	Convection velocity	CH 1: *Ionospheric currents*
Λ	Energy distribution function by Rees [1963, 1989]	CH 5: *ASCinv*
Λ_S	Energy distribution function by Sergienko and Ivanov [1993]	CH 5: *ASCinv*
Σ_H, Σ_P	Height-integrated Hall and Pedersen conductivities	CH 5: *Method of Characteristics*
α	Wave number along X (eastward)	CH 5: *Spiral model*
γ_H	Instability growth rate according to Hallinan [1976]	CH 5: *Spiral model*
γ	More general growth rate of the FAC instability	CH 5: *Spiral model*
ε	Energy deposition rate	CH 5: *ASCinv*
ν_{en}, ν_{in}	Neutral-electron and neutral-ion collision frequencies	CH 5: *Spectrum*
ξ	Hall-to-Pedersen conductance ratio	CH 5: *Method of Characteristics*
σ_H, σ_P	Hall and Pedersen conductivities	CH 5: *Spectrum*
ω_e, ω_i	Electron and ion gyrofrequencies	CH 5: *Spectrum*

LIST OF PUBLICATIONS

This thesis consists of an introduction and the following five publications:

I Partamies, N., Kauristie, K., Pulkkinen, T.I. and Brittnacher, M., **Statistical study of auroral spirals**, *Journal of Geophysical Research, 106*, 15415–15428, 2001.

II Partamies, N., Freeman, M.P. and Kauristie, K., **On the winding of auroral spirals: Interhemisphere observations and Hallinan's theory revisited**, *Journal of Geophysical Research, 106*, 28913–28924, 2001.

III Partamies, N., Amm, O., Kauristie, K., Pulkkinen, T.I. and Tanskanen, E., **A pseudo-breakup observation: Localized current wedge across the postmidnight auroral oval**, *Journal of Geophysical Research, 108*, doi:10.1029/2002JA009276, 2003.

IV Partamies, N., Janhunen, P., Kauristie, K., Sergienko, T., and Mäkinen, S., **Testing an inversion method for all-sky camera images**, *Annales Geophysicae, 22*, 1–11, 2004.

V Partamies, N., Donovan, E., Kauristie, K., and Janhunen, P., **An inversion method for all-sky images: A substorm study**, in Proceedings of the XXX Annual European Meeting on Atmospheric Studies by Optical Methods, 33–37, 2003.

1 INTRODUCTION

1.1 AURORA AND SPACE PLASMA PHYSICS

Auroral research belongs to the field of space plasma physics. Plasma is a gas of charged particles with equal numbers of negative and positive charges. Plasma processes are governed by electric and magnetic fields. In different environments – in the solar wind (interplanetary plasma), magnetosphere (near-Earth space) and ionosphere (the upper atmosphere) – plasma processes take place in different scale sizes. Global processes are studied by means of numerical simulations based on magnetohydrodynamic equations. The simulation results are evaluated by comparing them to in-situ satellite data or ground-based observations. The research of micro-scale processes uses theories on plasma instabilities driven by wave-particle interactions. Some of these processes have a crucial impact also on the evolution of global phenomena. The validation of small-scale features and their effect on more global processes is very challenging, but yet highly important. Recently launched and future ambitious satellite missions with high temporal and spatial resolution have been anticipated to show significant progress on this issue.

The research of ionospheric meso-scale (sizes from 10 to 1000 km) phenomena is the main area of this thesis. It includes determining the electrodynamic quantities and characteristics of particle precipitation with different methods from ground-based observations (magnetic field variations, auroral luminosity and radiowave backscatter). Our current understanding of the ionospheric electrodynamics has a profound observational basis, which is a significant advantage also in studies on the coupling between the magnetosphere and the ionosphere.

1.2 FROM THE SUN TO THE EARTH

The Sun is responsible for bringing the polar lights to the night sky of the arctic and antarctic regions. Activity on the Sun's surface controls the variability of the continuous outflow of plasma and the Interplanetary Magnetic Field (IMF). The charged particles of the solar wind are affected by the magnetic field of the Earth so that the plasma flow deviates around our planet as shown in Figure 1.1. The Earth's magnetosphere is a wind-sock shaped region governed by the Earth's magnetic field. The dynamic pressure of the solar wind squeezes the outer boundary of the magnetosphere, called magnetopause, towards the Earth on the Sun-facing side (dayside) to the point where it is balanced by the magnetic pressure of the Earth's magnetic field. On the nightside, the magnetic field becomes stretched into a tail-like configuration. The distance from the Earth to the dayside magnetopause is about 10 Earth radii ($R_E = 6371$ km) while the magnetotail reaches downstream up to 100 R_E and beyond. The distance from the Sun to the Earth is about 149 million kilometres (1 Astronomical Unit, AU) and the solar

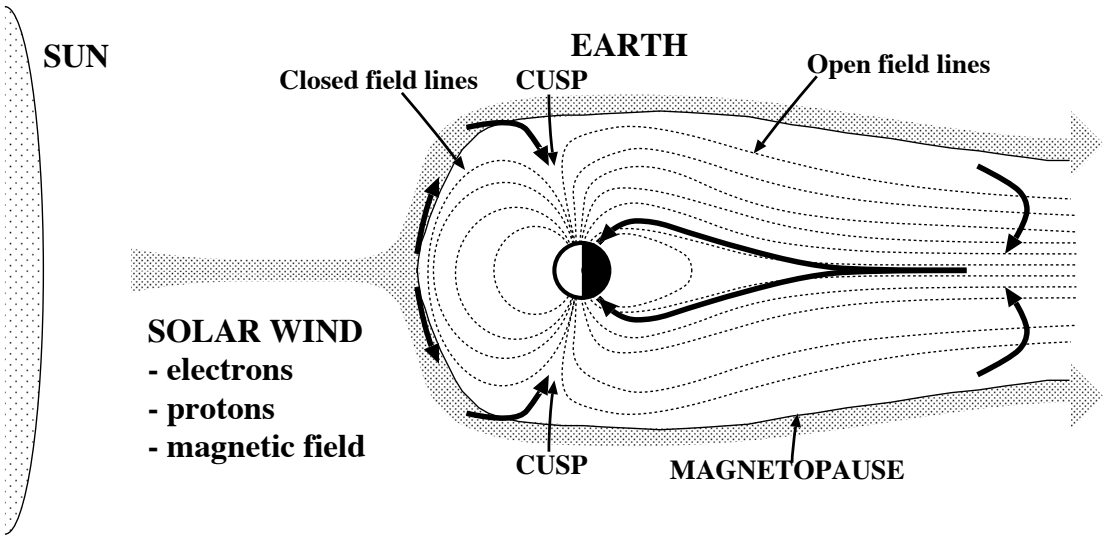

Figure 1.1. Interaction between the solar wind and the Earth's magnetic field. The arrows show the paths of the particles into the atmosphere through the dayside cusps and the magnetotail. Illustration by Mikko Syrjäsuo.

wind flows on average at the velocity of 400 km/s. Thus, the solar wind particles travel approximately four days away from the Sun to reach the Earth, but at the minimum they can make it in about ten hours.

The solar wind and the magnetospheric plasmas are mainly collisionless, i.e. the diffusion is negligible and plasma conductivity is infinite. In these conditions, the plasma moves together with the magnetic field; the plasma and the magnetic field are said to be frozen-in to each other. From the frozen-in, it follows that the solar wind plasma cannot freely enter the magnetosphere. One way for the solar wind particles to penetrate into the magnetosphere goes through the diffusion (reconnection) regions at the magnetopause where the frozen-in condition breaks. The dayside reconnection is followed by particle precipitation to the dayside ionosphere causing auroras in the regions called the cusps (see Figure 1.1). Part of the solar wind plasma may also be dragged down to the magnetotail along the tailward motion of the open field lines (see Section 1.4 and Figures 1.1 and 1.4), i.e. the magnetic field lines whose one end is attached to the Earth, the other being connected to the solar wind. The particles become stored in the tail to eventually be released partly downstream into the solar wind, partly to the nightside ionosphere to produce the auroral light. The regions where particles enter the ionosphere form nearly circular auroral zones around the magnetic poles of the Earth, the auroral ovals.

1.3 MAGNETOSPHERE

Figure 1.2 shows a sketch of the structure of the magnetosphere. The outer boundary of the magnetosphere, the magnetopause is governed by the magnetopause currents, also called Chapman-Ferraro currents on the dayside. On the nightside, the magnetopause

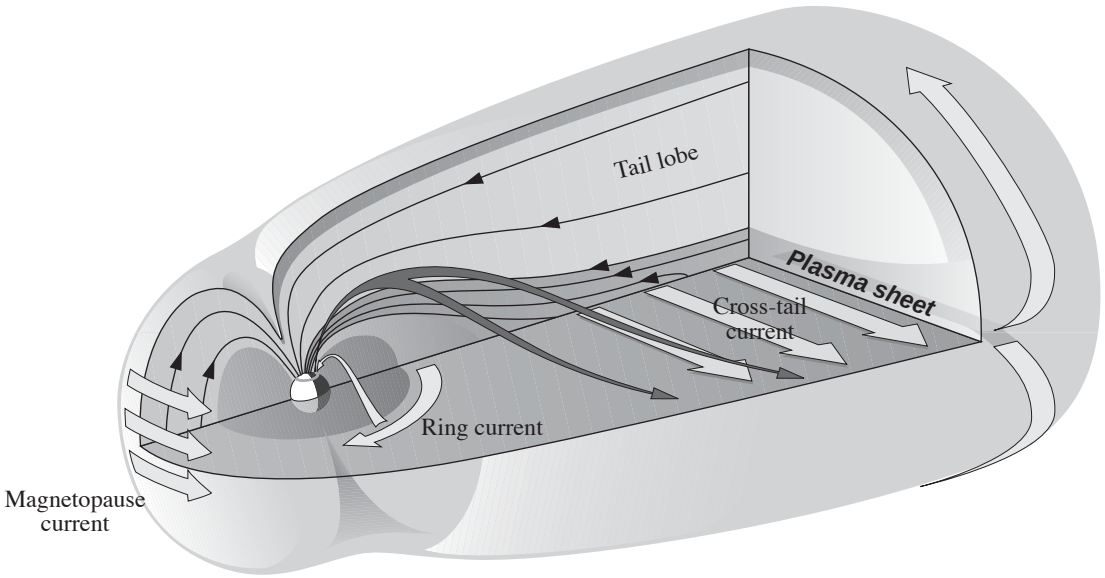

Figure 1.2. The most important current systems in the Earth's magnetosphere are the magnetopause current, the cross-tail current in the middle of the magnetotail and the ring current in the inner magnetosphere. Illustration by Teemu Mäkinen.

currents encircle the lobes of the magnetotail, where the magnetic field lines are open. The currents surrounding the tail lobes are closed by the dawn-dusk directed cross-tail current in the equatorial magnetotail. This cross-tail current region, called plasma sheet, consists of hot plasma and closed magnetic field lines (see Figure 1.1) with both ends connected to the Earth. The distribution and the time variations of the cross-tail current determine the magnetic field configuration between dipolar and tail-like, and it is highly involved in the dynamics of the magnetosphere (see Chapter 4). In the magnetotail, the plasma moves continuously from the tail lobes towards the centre of the plasma sheet as well as earthward inside the plasma sheet. This convective motion also reflects into plasma circulation in the ionosphere (see Section 1.4).

In the inner magnetosphere, the magnetic field is nearly dipolar. The main current system is called the ring current, which encircles the Earth in the vicinity of the geosynchronous orbit (at 6.6 R_E) and meets the earthward end of the plasma sheet on the nightside.

1.4 IONOSPHERIC CONVECTION AND CURRENTS

1.4.1 Structure of the ionosphere

The upper atmosphere above about 70 km is called the ionosphere, because it partly (about 0.1% of it) consists of charged particles, ions and electrons. Figure 1.3 summarises the structure (D, E and F-regions), the main ion composition of each region, and the main driver governing the ion and electron motion. Sketches of the conductivity profiles and the typical auroral altitudes (90–300 km) are illustrated, too.

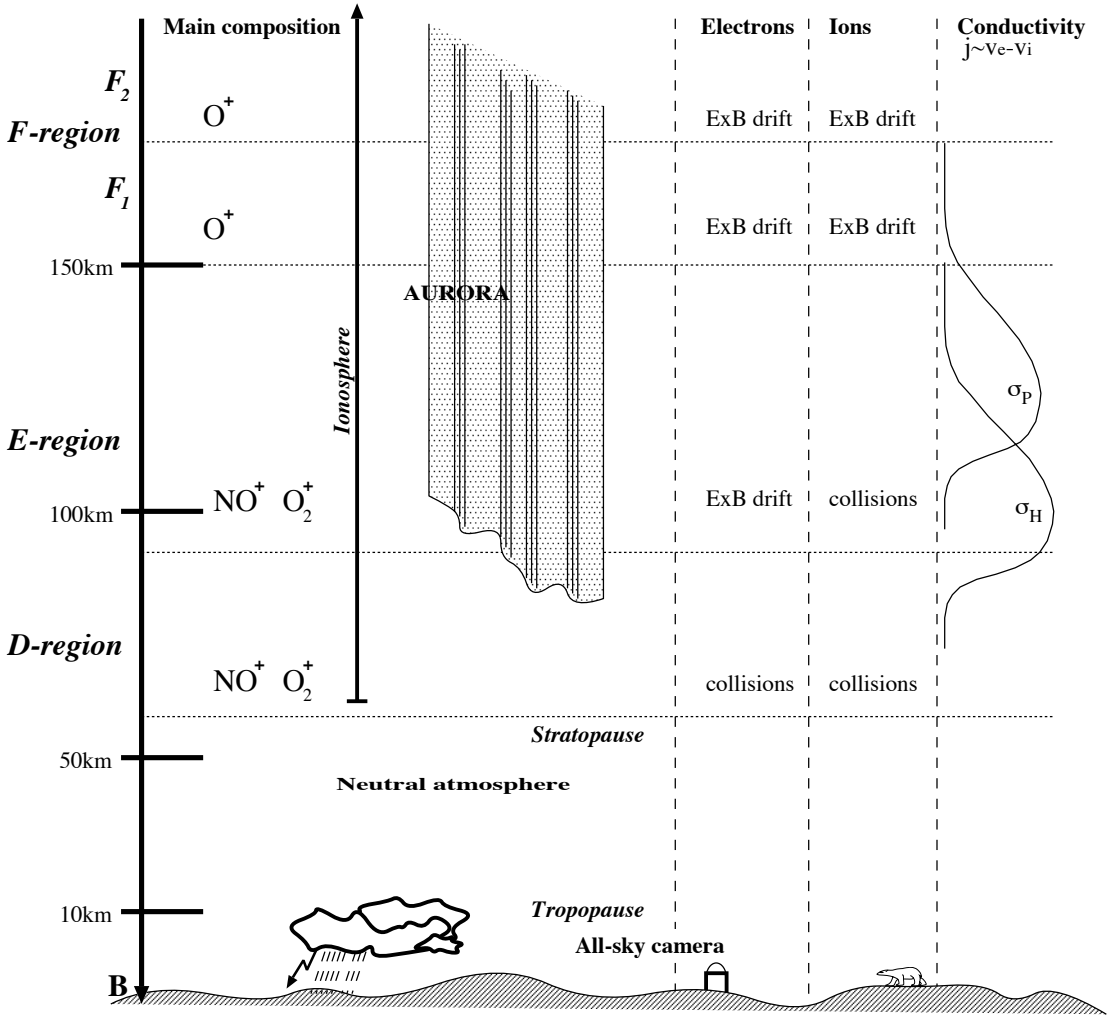

Figure 1.3. The regions and the main ion constituents of the ionosphere, the typical altitudes of the aurora as well as a sketch of the ionospheric Hall and Pedersen conductivity profiles. The main drivers of the ion and electron motion are also presented. Illustration by Mikko Syrjäsuo.

1.4.2 Convection

The magnetospheric convection results from the interaction between the magnetosphere and the solar wind at the magnetopause. In favourable conditions on the dayside magnetopause, the magnetic fields of the Earth and the solar wind are roughly oppositely directed and start to merge [Giovanelli, 1947; Priest and Forbes, 1986] speeding up the convection. The outermost closed field lines open and the newly opened field lines drift tailward (antisunward) along the solar wind (see Figure 1.4a). Closer to the centre of the magnetotail the open lobe field lines are closed again by the nightside reconnection. The return flow of the closed field lines to the dayside (sunward) takes place in the inner magnetosphere corresponding to lower latitudes in the ionosphere (see Figure 1.4b).

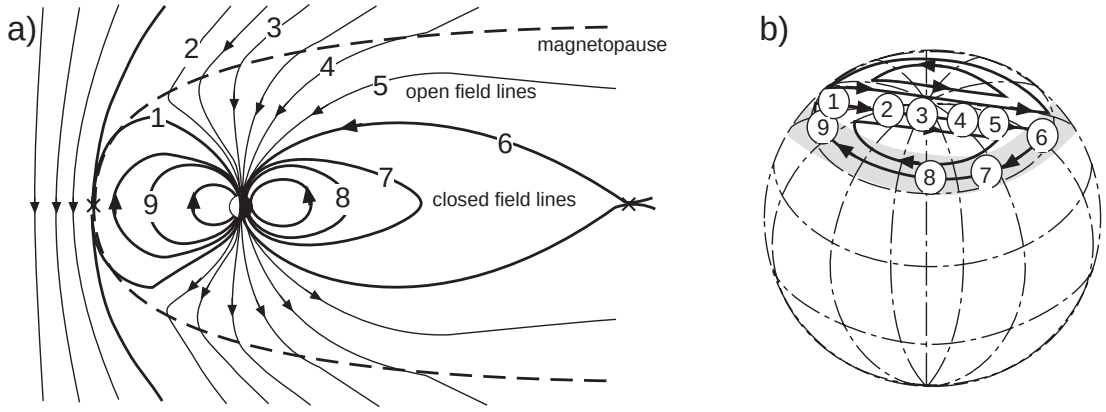

Figure 1.4. Magnetospheric convection (a) and the corresponding plasma motion as mapped into the ionosphere (b). The numbers indicate the motion of a single magnetic field line along its convection cycle. Illustration by Minna Palmroth, after Dungey [1961].

The magnetic field of the Earth together with the motion in the collisionless plasma of the solar wind produce an electric field $\mathbf{E} = -\mathbf{v} \times \mathbf{B}$. In case of the antisunward directed flow and the earthward magnetic field, the electric field points from the dawn to the dusk. As the magnetic field lines are equipotentials and the plasma is free to move along them, the magnetospheric potential pattern is projected to the ionosphere (see Figure 1.4b and Figure 1.5). The dawn-to-dusk electric field maps down to the region of antisunward flow as a polar cap electric field ($\mathbf{E}_{\mathrm{PC}}$). The sunward return flow on the evening (morning) side is accompanied by a poleward (equatorward) directed electric field (see Figure 1.5).

Since the magnetospheric convection is driven by the solar wind, also the ionospheric convection responds to the solar wind changes. For instance, changes in the sign of the dawnward component of the IMF will move the dayside reconnection region in the azimuthal direction and correspondingly tilt the antisunward flow. The two-cell convection described by Figure 1.5 is an ideal static situation, and the observed flow pattern (as shown in, e.g., http://superdarn.jhuapl.edu/rt/map/) is highly variable in both

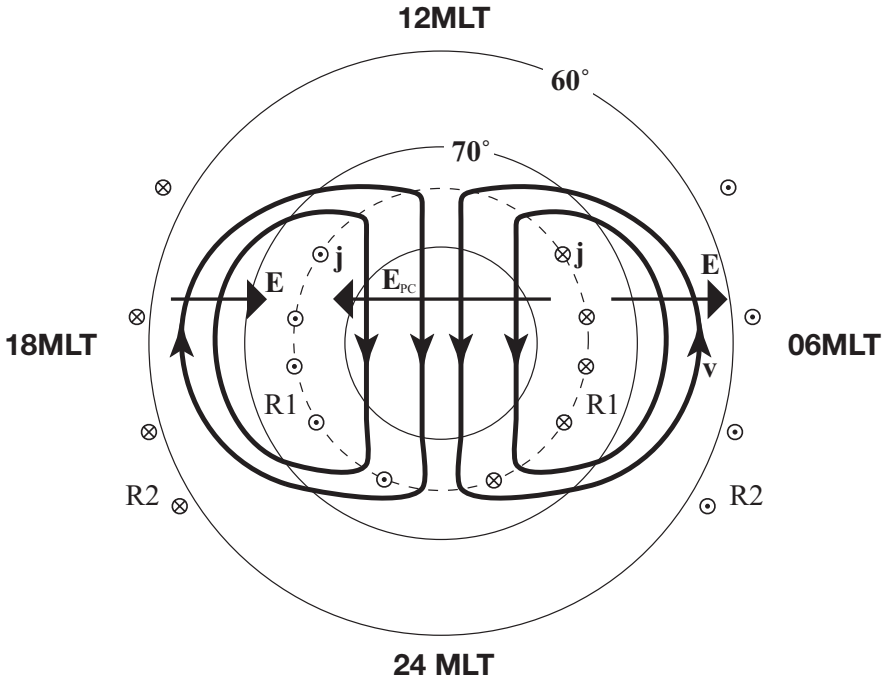

Figure 1.5. An ideal view of the ionospheric convection pattern from above the northern hemisphere shows the average locations of the plasma flow **v**, electric fields **E** and field-aligned currents **j**. The inner and outer field-aligned current regions are marked by R1 and R2. $\mathbf{E}_{\mathrm{PC}}$ stands for the polar cap electric field and the latitudes refer to the geomagnetic latitudes encircling the geomagnetic pole. The dashed circle indicates the open-closed field line boundary, i.e. the boundary of the polar cap. Illustration by Mikko Syrjäsuo, after Heppner and Maynard [1987].

flow intensity (strength of the polar cap potential and $\mathbf{E}_{\mathrm{PC}}$) and configuration (2–4 flow cells of different size). Measurements of the ionospheric convection are provided, for instance, by ionospheric radars (see Chapter 2), but the convection can also be indirectly estimated from magnetometer recordings in the plasma flow region. In addition to the changes in the solar wind, the Ultra-Violet (UV) radiation of the Sun affects the potential pattern. The ionisation due to the solar UV results in a conductivity gradient from the dayside to the nightside and thus, in an additional electric field, which rotates the flow pattern (not taken into account in Figure 1.5).

1.4.3 Currents

The large-scale field-aligned currents (FAC) associated with the convection consist of two regions marked in Figure 1.5 [Iijima and Potemra, 1978, 1976a]. Region 1 (R1) currents are located inside the evening and morning flow cells, while Region 2 (R2) currents flow at lower latitudes and are spread out to a larger area. The convergence

of the electric field is related to the upward FAC in the R1 area inside the evening cell and the electric field divergence is associated with the downward FAC in the morning R1 area. In the ionosphere, the R1 and R2 currents are closed via horizontal Pedersen currents flowing parallel to the electric fields. The magnetospheric end of the R1 currents are connected to the currents at the outer magnetospheric boundaries while the R2 currents are coupled to the partial ring current in the inner magnetosphere (e.g. McPherron [1991]). In the ionosphere, the FACs arise from the conductivity gradients and variations in the electric fields. In the magnetosphere, the FACs are fed by the pressure gradients [Birmingham, 1992b] and the vorticity of the plasma motion.

The auroral electrojets are located within the convection return flow region (see Figure 1.5) flowing westward on the morning and eastward on the evening side. Being perpendicular to the ionospheric convection electric fields, these currents are called Hall currents (see, Chapter 5). The transition region from the eastward to the westward electrojet in the midnight sector is also a region of an electric field reversal (not shown in the idealised convection of the Figure 1.5). It is named Harang Discontinuity (HD) [Heppner, 1972], and there are many interesting physical phenomena, such as strong upward FACs, related to it. Although the statistical HD pattern has been resolved [Harang, 1946; Heppner, 1972], its instantaneous appearance in different conditions is still an open issue [Amm et al., 2000].

Meso-scale current systems related to different structures in the aurora are discussed in Chapter 3.

1.5 AURORAL LIGHT

The auroral ovals encircle the magnetic poles on both hemispheres at the average magnetic latitudes of 60°–75°, being narrower and at higher latitudes on the dayside than on the nightside. They are also roughly co-located with the sunward return flow of the convection (see Figure 1.5) and the electrojet region.

The coupling between the magnetosphere and the ionosphere through field-aligned currents, particle precipitation and convection as explained above, is the link that provides us with a view to the magnetosphere from the ground. The electrons precipitating into the Earth's atmosphere carry upward FACs and are responsible for the production of the auroral light. When the electrons penetrate into the ionosphere they collide with the atmospheric constituents (e.g. oxygen atoms and nitrogen molecules). In the collisions, the atmospheric particles gain energy and excite. The release of this extra energy results in light observed as the aurora. Emissions at the X-ray, ultra-violet and infra-red wavelengths are also produced but this thesis concentrates on the visual wavelengths of the aurora.

Particles responsible for the visual aurora have typically energies of 0.5–20 keV and they produce auroral emission with intensities of about 5–50 kR (e.g. Brekke and Egeland [1994]), where Rayleigh (R) is a photon flux of 10^{10} photons/m^{2}s. The

main colours observed in the aurora are red (630.0 nm), green (557.7 nm) and blue (427.8 nm). The two former are produced by the electron collisions with the atomic oxygen while the latter is due to collisions with nitrogen molecules. Green emission is the most common and the strongest one within the nightside aurora. Red emission is as common but much weaker than the green emission and thus, it is more rarely picked out by a human observer from an auroral display dominated by the green light. The excitation energies of the atmospheric species are low ($\leq$100 eV, e.g. Rees [1989]) compared to the initial energies of the precipitating particles. Thus, the electrons undergo many collisions before producing light and only about 1-2$\%$ of their energy goes to the light production [Brekke and Egeland, 1994]. In addition to the ionisation and light production, part of the energy of the precipitating electrons heats the ambient electron gas and adds to the kinetic energy of the neutral gas. Secondary electrons are electrons set free in the ionisation by the precipitating particles. Their energies are low but enough to produce emission, especially red light. Diffuse red emission is typically due to electrons with initial energies less than 1 keV and thus, the contribution of the secondary electrons is significant in the red auroral light. Green and blue emissions are produced by higher energy particles capable of penetrating deeper to the atmosphere. Quenching of the atomic oxygen before emission prohibits the formation of the red aurora at low altitudes. Details of each emission are summarised in Table 1.1. All these

Table 1.1 Some details of the most typical auroral emissions [Brekke, 1997].

Emission	RED	GREEN	BLUE
Wavelength (nm)	630.0	557.7	427.8
Lifetime	107 s	0.7 s	70 ns
Excited state	O^{1D}	O^{1S}	N_2^+
Peak altitude (km)	250	110	90

three wavelengths are recorded by MIRACLE all-sky cameras (see Chapter 2) through narrow band-pass filters and are extensively used in this thesis.

The proton emission (H^+) at the wavelength of 486.1 nm is much weaker than the electron aurora (50–300 R). It is usually measured by photometers, which are more sensitive than auroral imagers. Proton auroras are dominant on the dayside and characteristic to the ionospheric footpoint of the cusps, but they are detectable within the nightside aurora, too. The nightside proton precipitation has its origin in the plasma sheet and thus, it can be used to track the changes in the plasma sheet thickness. This in turn, is related to the substorm dynamics (see Chapter 4).

2 INSTRUMENTATION

2.1 MIRACLE INSTRUMENT NETWORK

2.1.1 Overview

The observations of the Magnetometers — Ionospheric Radars — All-sky Cameras Large Experiment (MIRACLE) ground-based instrument network form the core of this thesis. It currently consists of 28 magnetometers, 8 all-sky cameras and a coherent scatter radar in Northern-Fennoscandia and on Svalbard as shown by Figure 2.1. This network is operated as an international collaboration under the leadership of the

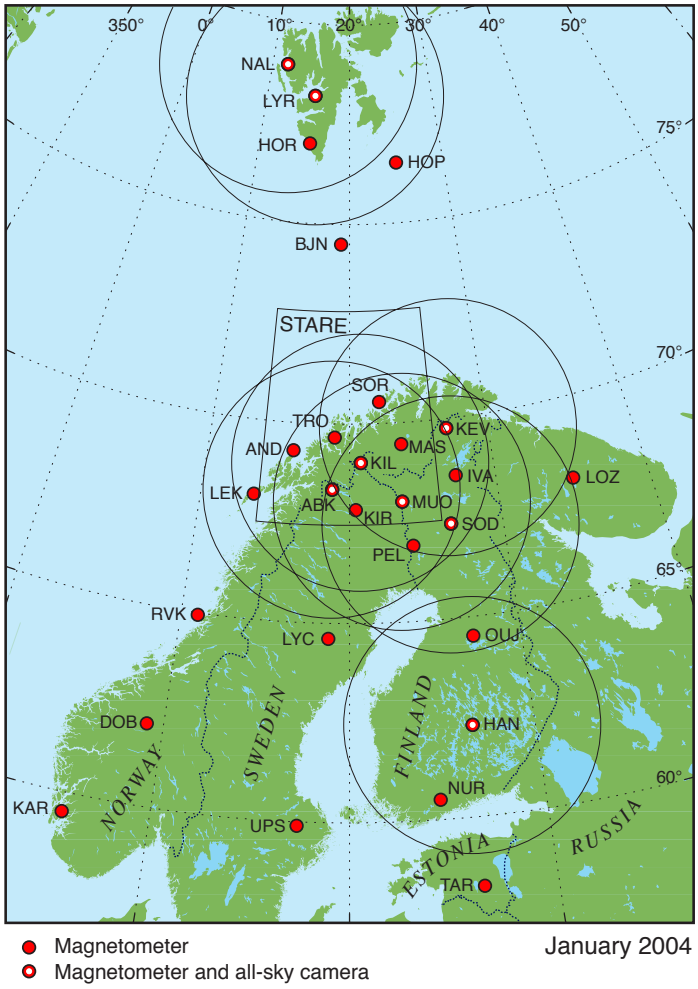

Figure 2.1. Locations of the IMAGE magnetometer stations, the common field-of-view of the STARE radar (rectangle) and ASC field-of-views (circles). Illustration by Lasse Häkkinen.

Finnish Meteorological Institute. It was designed for two-dimensional meso-scale (10–1000 km) studies of the aurora, which is also how it has been utilised in this thesis in

the studies of auroral spirals, arcs and breakups. The MIRACLE concept of an extensive magnetometer network combined with two-dimensional electric field and auroral observations enables us to apply various data analysis methods to these data and to study the dynamics and morphology of the ionospheric electric and magnetic fields, the electric currents and conductivities.

The following sections contain brief descriptions of the instruments included in MIRACLE.

2.1.2 All-sky cameras

Finnish Meteorological Institute has used digital All-Sky Cameras (ASC) to monitor the aurora since 1996. They operate automatically whenever it is dark enough, i.e. every winter night from about September to mid-April. The fish-eye lens provides a Field-Of-View (FOV) of about 180°. The station configuration and some specific parts of the camera are introduced in Figure 2.2. A detailed description of the camera

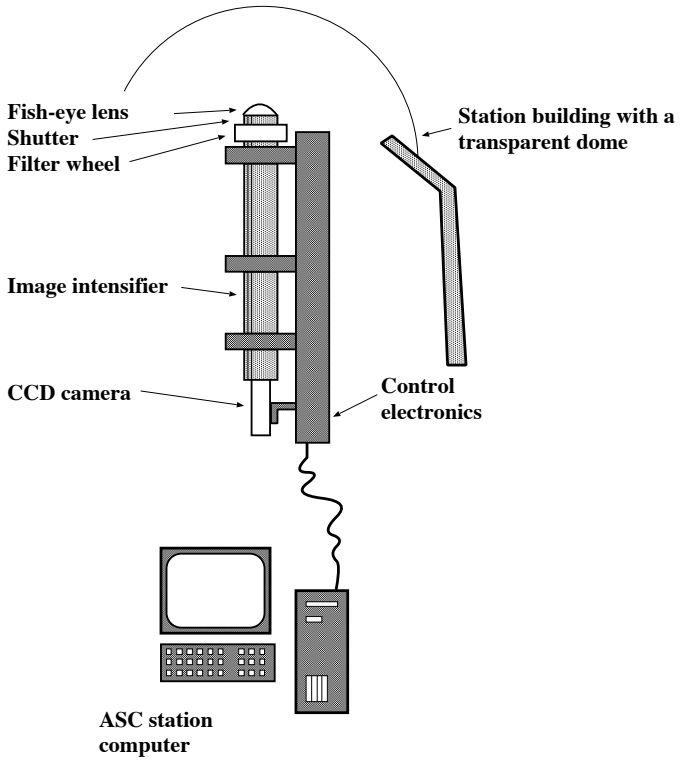

Figure 2.2. MIRACLE ASC installation. In front of the image capturing CCD (Charge Coupled Device) there are the fish-eye lens to capture the view of the whole sky at once, the shutter, filter wheel with green, red and blue line filters and the image intensifier to intensify the signal to the level the CCD is sensitive to. The camera looks directly to the zenith through the dome. The system is controlled by a computer and is capable of operating on its own. [Syrjäsuo, 2001]

network, its history and operation can be found in Syrjäsuo [2001].

ASC observations have a key role in this work. ASCs have been used to capture images of auroral meso-scale structures that are introduced in the next chapter and discussed in more detail in PUBL. I, PUBL. II and PUBL. III. Regular intensity calibrations of the ASCs were started in the summer of 2001 [Mäkinen, 2001] enabling the conversion of digital units of the images to absolute brightness values in Rayleighs. This step was necessary for testing of the inversion method by Janhunen [2001] (for more details, see Chapter 6) as presented in PUBL. IV and PUBL. V.

2.1.3 Magnetometers

The MIRACLE network includes the International Monitor for Auroral Geomagnetic Effects (IMAGE) magnetometer network (see Figure 2.1). This chain of 28 fluxgate magnetometers covers the latitudes from 58°N to 79°N (54°–75° in magnetic latitude) measuring the changes in the geomagnetic field (in X, Y and Z components, which are positive towards the geographic north, east, and downward, respectively). IMAGE is especially useful in studies on the auroral electrojets and evolving two-dimensional current systems, as in the event reported in PUBL. III.

2.1.4 STARE

Scandinavian Twin Auroral Radar Experiment (STARE) [Greenwald et al., 1978] consists of two coherent radars (one in Hankasalmi, Finland and one in Midtsandan, Norway), whose common rectangular FOV covers the region between 14°–26°E longitude and 68°–73°N latitude (see Figure 2.1). The operating frequency of these radars ($\sim$ 140 MHz) is suitable for probing the speed of the metre-scale irregularities in the E-region ionosphere as sketched in Figure 2.3. The irregularities are changes in the ionospheric electron density caused by varying electric fields of waves and instabilities. Because the conductivity along the geomagnetic field lines is very high and the particles are free to move in this direction, the irregularities will smooth out quickly. As a consequence, the density structures are nearly field-aligned and scatter radiowaves with wave vectors perpendicular to them in a way analogous to the Bragg scattering (transmitted wavelength is proportional to the double of the distance between the consecutive density maxima). Field-aligned irregularities are assumed to drift along the ionospheric convection and thus, the Doppler shift of the signal scattered by the irregularities reveals the Line-Of-Sight (LOS) component of the convection velocity. When two radars are operated simultaneously, the combination of their measurements from the common FOV will give the horizontal plasma velocity. Furthermore, by assuming an $\mathbf{E} \times \mathbf{B}$-drift and an earthward magnetic field, the velocities measured by STARE can be used to estimate the ionospheric electric fields.

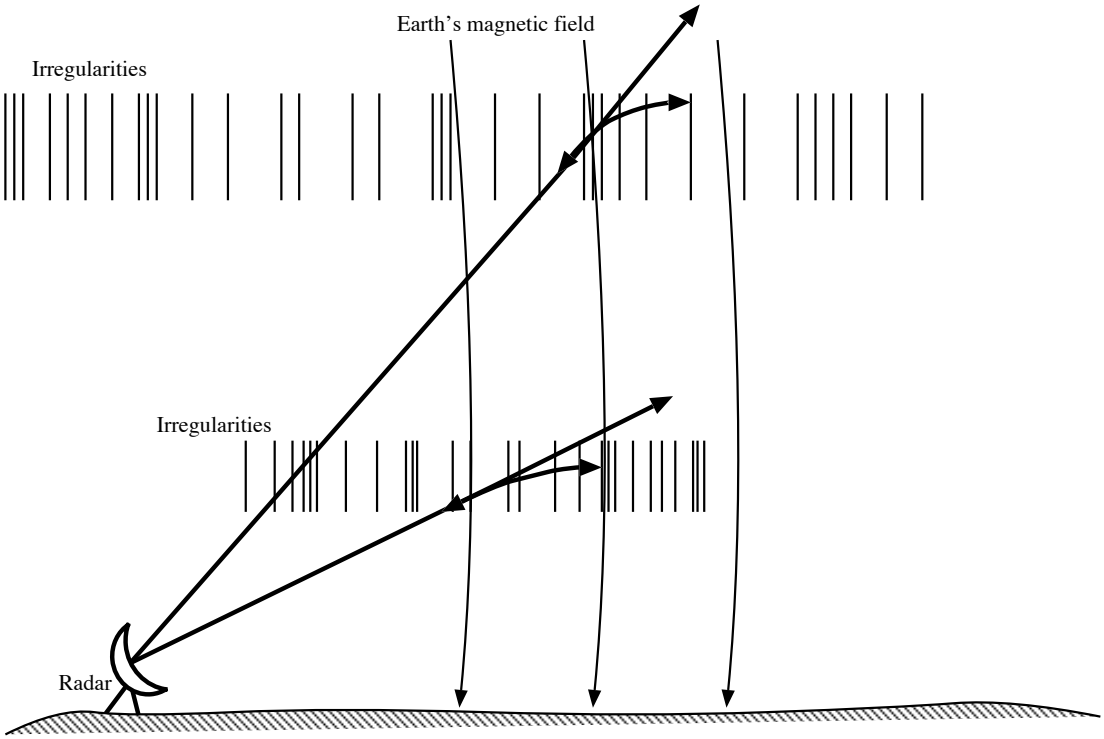

Figure 2.3. Operation of coherent scatter radars. Radiowaves are scattered by the field-aligned electron density variations called irregularities. The scattering process follows the Bragg's law. Illustration by Mikko Syrjäsuo.

The STARE measurements are restricted to the periods when the ionospheric electric field exceeds about 15 mV/m. This threshold electric field arises from the velocity difference between the Hall-drifting (perpendicular to $\mathbf{E}$) electrons and collision-dominated ions, which is necessary for the formation of the E-region instabilities, and thus irregularities . In general, this condition is satisfied within the auroral electrojet region but is violated in the regions of intense precipitation, high conductivity and consequently, low electric field. Another limitation of STARE is that the phase velocity of the irregularities is actually observed to differ from the $\mathbf{E} \times \mathbf{B}$ direction by about 5°–15° [Uspensky et al., 2003]. This was originally reported by Nielsen and Schlegel [1983] as an underestimation of the drift velocity. It arises from the fact that the colliding ions alter the direction of the electron drift. Nielsen and Schlegel [1985] and Uspensky et al. [2003] have presented techniques to overcome this problem.

Despite the problems mentioned above, the ionospheric plasma flow recordings by STARE have been important in studies on evolving auroral forms, such as in the event studied in PUBL. III, especially because the temporal resolution of the STARE data is as good as 20 s. The electric field, in turn, allows the usage of the Method of Characteristics [Amm, 1995] for solving the ionospheric conductances as well as the horizontal and field-aligned currents (for more details see Chapter 5). The conductances defined by the Method of Characteristics are in a good agreement with the ones deduced

from the space-borne X-ray images of the aurora (e.g. Aksnes et al. [2004]).

2.2 OTHER INSTRUMENTS

2.2.1 EISCAT radars

The European Incoherent SCATter (EISCAT) radars [Risbeth and van Eyken, 1993] are internationally maintained and operated instruments in Tromsø in the mainland Norway and in Longyearbyen on Svalbard. These radars use the radio frequencies of 500 MHz (Ultra High Frequency (UHF) radar on Svalbard), 930 MHz (UHF radar in Tromsø) and 224 MHz (Very High Frequency (VHF) radar in Tromsø) for sounding thermally excited ionospheric ion-acoustic waves of a few kHz. They record backscatter from the electrons along the radar beam, which crosses the ionospheric D, E and F-regions up to the altitude of about 1000 km. The word incoherent is slightly misleading in this con-

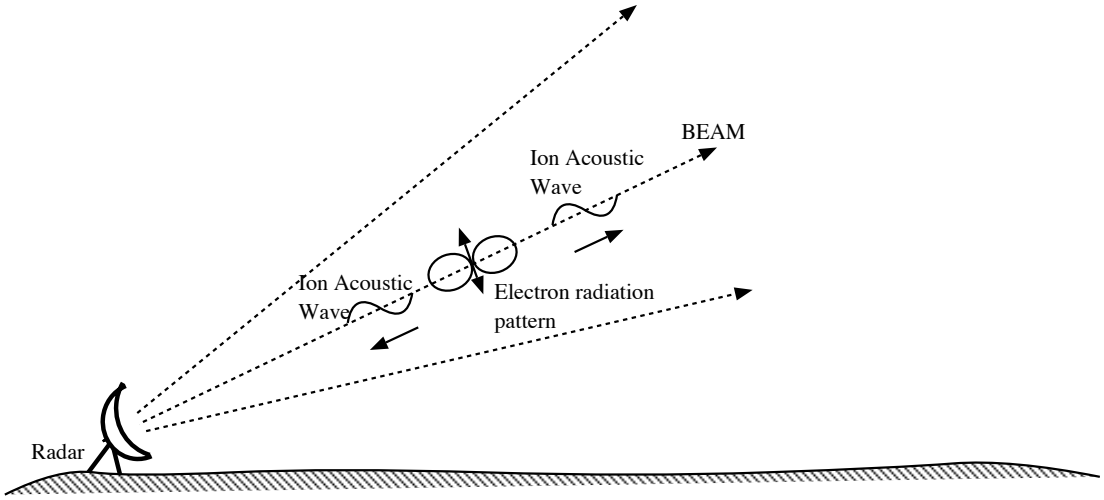

Figure 2.4. Schematic of view of the operation of incoherent scatter radars. Radiowaves are scattered by single electrons, the electrons are coupled to the ions and the ions are moved by the ion-acoustic waves. The scattering from the individual electrons is Thomson scattering. Again, illustration by Mikko Syrjäsuo.

text: although the radiowaves are scattered by single electrons as Thomson scattering (see Figure 2.4), the motion of the electrons is governed by the thermal movements of the heavier ions. In this sense, the scattering is coherent. The ion motion is determined by the ion-acoustic waves, of which the ones propagating along the radar beam (away and towards) are detected.

The backscattered signal is very weak, but with advanced analysis methods [Nygrén, 1994] electron density, ion velocity as well as electron and ion temperatures can be deduced from the power, position and the shape of the spectrum of the backscattered signal. The electron density is proportional to the total power received. The shift of

the received frequency from the transmitted frequency corresponds to the bulk plasma velocity (ion drift). In addition, ion and electron temperatures can be deduced from the spectrum of the received signal. The electron density profiles can also be used to calculate conductivities as well as to invert precipitating energy and number fluxes with, for example, a Spectrum programme [Kirkwood, 1988] introduced in Chapter 5. Electric fields can be estimated from the radar recordings, too. This requires simultaneous common volume measurements from the radars in Tromsø, Sodankylä and Kiruna, or a single radar scanning between a few points around a fixed position with a long enough integration time.

The ion temperature and electron density measurements have been used to determine the regions of strong ionospheric electric fields (frictional heating, e.g. Rees [1989]; Davies et al. [1995]) in PUBL. III. The same study also shows a comparison between conductivities derived from the EISCAT measurements and the ones solved by the Method of Characteristics (see Chapter 5).

2.2.2 Satellites

The satellite data used in this thesis are mainly particle measurements from different parts of the near-Earth space. The satellite measurements include solar wind monitoring (particles, fields, solar wind speed and pressure), e.g. by the Advanced Composition Explorer (ACE) satellite, energetic particle detection at the geosynchronous orbit by the Los Alamos National Laboratory (LANL) instrumentation, auroral oval imaging (in visual and UV wavelengths) by the high-altitude Polar satellite and particle detection by the low-altitude Defense Meteorological Satellite Program (DMSP) satellites. The orbital information, instrument or measurement of interest as well as a reference for each of them are listed in Table 2.1.

Table 2.1 Listing of the satellites used in the thesis. The L1 point is located at the Earth-Sun line at the distance of about $1.5 \cdot 10^6$ km from the Earth.

Satellite	ACE	LANL	Polar	DMSP
Orbit	L1 point	geosynch. orbit at 6.6 R_E	altitude of 1.8–9 R_E	altitude of 800 km
Measurements of interest	particles (SWEPAM) & fields (MAG)	energetic particles	UVI images	particles (SSJ/4)
Reference	McComas et al. [1998] Smith et al. [1998]	Higbie et al. [1978] Belian et al. [1978]	Torr et al. [1995]	Hardy et al. [1984]

3 OBSERVATIONS OF DIFFERENT AURORAL STRUCTURES

3.1 AURORAL ARCS

This chapter will introduce some of the meso-scale auroral structures, which are found embedded at the electrojet latitudes of the auroral oval.

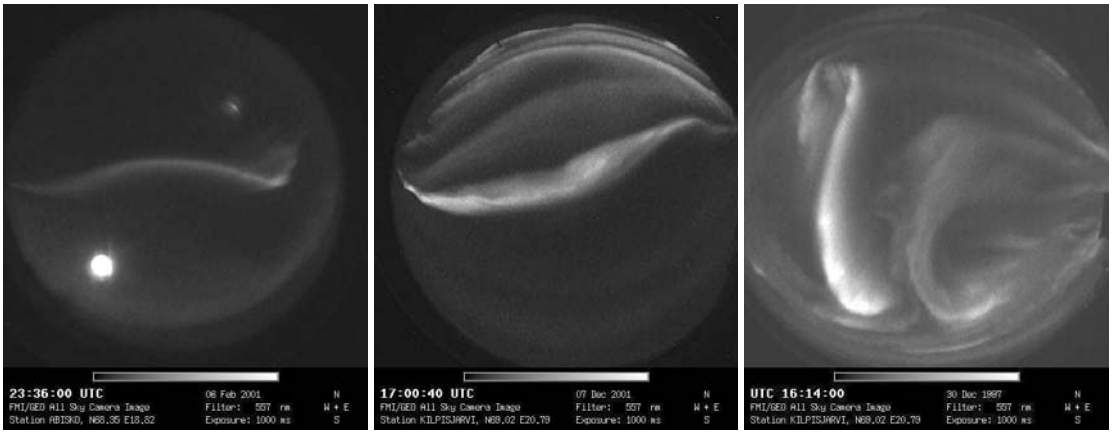

Figure 3.1. ASC images of auroral arcs at 557.7 nm. A single arc is shown on the left, multiple arcs in the middle and a north-south aligned arc on the right. The bright spot on the leftmost image is the Moon and the dimmer spot on the opposite side of the same image is the reflection of the Moon from the dome. The image captions include the time, date, station and its location, filter, exposure time and the compass. The FOV of these images corresponds to a circle with a diameter of about 600 km at the altitude of 110 km.

An auroral arc is the simplest and most common auroral form (see Figure 3.1). Quiet east-west aligned stable arcs are often observed during weak magnetic activity while folding arcs are more likely related to the beginning of the expansion of an auroral substorm (see Chapter 4). Understanding of the arc formation mechanisms and its electrodynamics (e.g. Borovsky [1993]; Knudsen et al. [2001]; Aikio et al. [2002]; del Pozo et al. [2002]; Janhunen and Olsson [2002]) can be used as a starting point for the research of more complicated auroral structures. The arcs that appear fairly stable both in place and intensity in the MIRACLE data also provide a platform for testing new data analysis methods such as the inversion method (more in Chapter 5) studied in PUBL. IV and PUBL. V.

The east-west (along the oval) length of an arc may be hundreds of kilometres but its north-south (across the oval) dimension varies from a few hundreds of metres to some tens of kilometres (e.g. Borovsky [1993]; Knudsen et al. [2001]). Due to the electron precipitation associated with the arcs, they are also accompanied by upward FACs. As the current continuity must hold everywhere in the ionosphere, the corresponding downward current is found on equatorward side of an evening arc and on

the poleward side of a morning arc. To complete the current closure, arc-related horizontal electric fields (e.g. Aikio et al. [1993]) on the equatorward (poleward) side of an evening (morning) sector arc drive Pedersen (parallel to **E**) currents towards the arc. These fields are directed parallel to the large-scale ionospheric convection electric fields (described in Chapter 1.4) intensifying them on the equatorward (poleward) side of the evening sector arc. A significant part of the electrodynamics of the arcs is resolved by analysing the EISCAT radar measurements and narrow-angle high resolution imager data (e.g. Aikio et al. [2002]; del Pozo et al. [2002]; Lanchester et al. [1997, 2002]).

In addition to the electron precipitation, arcs are often associated with a field-aligned potential structure above the altitude of about 1 R_E. The potential drop accelerates the earthward precipitating electrons [Evans, 1974]. The simplest case of U-shaped potential and upward electric field is not enough to explain the observed precipitation characteristics in all occasions [Janhunen and Olsson, 2000], and the exact mechanisms maintaining the potential drops are still under debate.

3.2 ARC DISTORTIONS: FOLDS, SPIRALS, CURLS

The distortions in auroral arcs often appear as folds, spirals and curls. This classification is based on the size and lifetime, sense of rotation and reversibility of these structures. The two former categories are considered as meso-scale features and are often found in the ASC data as shown by Figure 3.2. The last group presents fine-scale au-

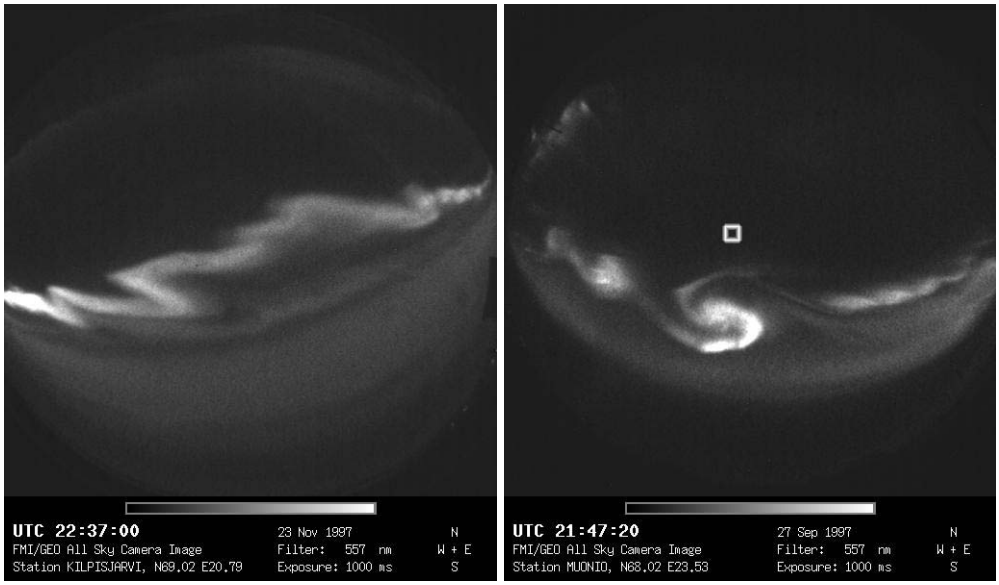

Figure 3.2. Examples of multiple folds (left) and spirals (right) within a single distorted arc. The white box in the spiral image corresponds to the FOV of the (trans)portable imager used for curl capturing. An example of a curl is shown in Figure 3.4.

roras with sizes beyond the spatial resolution of an ASC [Trondsen and Cogger, 1998] (see Figures 3.2 and 3.4).

The diameter of a spiral typically varies from 20 km to 1500 km [Davis and Hallinan, 1976]. The largest spirals are too large to be observed by a single ASC with the FOV diameter of about 600 km. The winding direction of these structures is always counterclockwise when viewed along the magnetic field, and they are often reversible. Spirals occur as single structures or as a spiral street of multiple disturbances in a single arc. The statistical appearance of the spirals is studied in PUBL. I, and their formation in PUBL. II (see also Chapter 5). The statistical analysis of about 200 well-defined spiral forms showed that the spiral observations are evenly distributed in pre- and post-midnight sectors. These structures also tend to move along the ionospheric convection, i.e. eastward (westward) on the morning (evening) side. Their observed speeds are of the order of a few km/s, which is comparable to the velocities of other auroral forms such as folds [Davis and Hallinan, 1970], westward travelling surges [Akasofu, 1964; Koskinen et al., 1990] and azimuthally spaced auroral forms [Elphinstone et al., 1996]. The spirals can equally well be related to very weak or relatively strong magnetic activity. Compared to the spiral observations from the satellites [Davis and Hallinan, 1976], the ASC observations can capture smaller structures. The larger and probably more torn forms are likely to take place within stronger magnetic activity, during pseudo-breakups and substorms.

Folds are tilted in the direction of the spiral winding, but their dimensions are smaller, of the order of some tens of kilometres. They are believed to be caused by the same mechanism as the spirals [Hallinan, 1976], i.e. a field-aligned current instability (more in Chapter 5 and in PUBL. II). In this scenario a fold appears as a middle stage between a smooth arc and a completely wound spiral.

Curl diameters extend from a couple of kilometres to about 10 km at the maximum. Their winding direction is opposite to that of the spirals and folds, i.e. clockwise along the magnetic field, and they are only able to wind, not unwind. An exception of a reversible curl with an opposite winding direction has been reported by Lanchester et al. [1997]. One of the suggested mechanisms to generate curls is a Kelvin-Helmholtz type shear flow across the underlying arc [Davis and Hallinan, 1970] as shown by Figure 3.3. Assuming the $\mathbf{E} \times \mathbf{B}$-drift applies, the direction of the shear flow is tied to the direction of the background magnetic field. In this approach, the irreversible nature of these forms then follows from the constant sign of the background magnetic field, which does not allow the shear to turn. This, however, does not explain an opposite sense of rotation and is not applicable to a reversible structure. Figure 3.4 shows an example of the curl observation by a narrow FOV portable auroral imager with high temporal (30 frames per second) and spatial (100 m) resolution [Trondsen and Cogger, 1998].

Both observations and theoretical models suggest that all these smaller structures are related to enhancements of the upward FAC within the underlying arc (for spirals e.g. PUBL. III, for folds e.g. Lanchester and Rees [1987] and for curls Burke et al. [1983]). Resolving the distribution of the downward FAC closing the upward currents

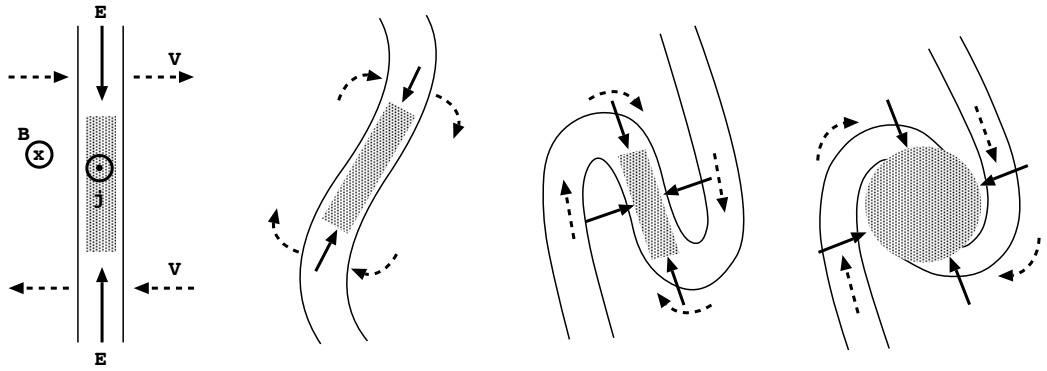

Figure 3.3. Formation of curls as presented by Davis and Hallinan [1970]. Solid arrows mark the electric field related to the electron precipitation within the arc (shaded area) and dashed arrows indicate the direction of the $\mathbf{E} \times \mathbf{B}$-drift, which works to bend the arc into a vortex.

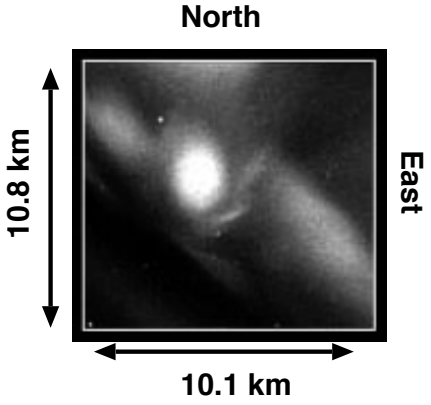

Figure 3.4. An example image of an auroral curl, which corresponds to a square of 10.1 times 10.8 km (opening angle of 5–6°) at the altitude of 105 km. This curl is viewed from below so that north is up and east is to the right in the image. The integration time of the imager is 17 ms [Trondsen and Cogger, 1998].

in the vortex surroundings still needs further studies with high resolution satellite observations. The term black aurora [Røyrvik, 1976] has been used in the literature for well-defined dark regions within diffuse aurora. Satellite data suggest that black aurora is associated with downward FAC [Marklund et al., 1997]. The intuitive conclusion from such observations would be that the FACs close locally and in case of a spiral the upward and downward FACs would roughly balance each other as integrated over the structure. However, the analysis of the current distribution of a spiral in PUBL. III shows that the main part of the downward current is located in the region further away from the spiral.

4 AURORAL ACTIVITY

4.1 SUBSTORM AND ITS SIGNATURES FROM THE GROUND

The concept of an auroral substorm was first defined by a systematic analysis of a vast amount of all-sky camera recordings by Akasofu [1964]. Although the individual auroral displays showed great variability, Akasofu noticed a systematic behaviour in the time evolution from one display to another. To make a distinction to the term geomagnetic storm, which is used for a longer period (days) of strong geomagnetic activity (e.g. Gonzales and Tsurutani [1987]), he called the sequence a substorm. The two phases of the substorm were named expansion and recovery. Later on, data from several ground-based magnetometer networks suggested that the expansion phase is often preceded by a gradual decrease of the horizontal magnetic field component. This growth phase [McPherron, 1970] was previously included in the first stage of the expansion phase in the definition by Akasofu.

The auroral display of the growth phase typically contains a series of equatorward moving arcs [Akasofu, 1964; Pulkkinen et al., 1991] (the two first rows of the Figure 4.1). The equatorward motion of the whole nightside auroral oval, especially the proton emission, can also be observed. The auroral electrojets strengthen causing a gradual negative excursion of the X-component of the ground-based magnetic field in the region of the westward electrojet, as shown in Figure 4.2. Correspondingly, a positive excursion appears in the afternoon sector under the eastward jet.

In the global view, the substorm growth phase is considered to begin when the Z-component of the interplanetary magnetic field (IMF B_Z) turns south (negative) [Aubry et al., 1970]. The dayside reconnection opens a more efficient way for energy and particle transfer from the solar wind into the magnetosphere. Consequently, the polar cap becomes wider, convection enhances and thus, the convection electric fields become stronger. The newly opened field lines cross the polar cap (the antisunward flow in Figure 1.5) ending up to the lobes of the magnetotail. When the tail lobes are building up, the magnetotail stretches, the cross-tail current (see Figure 4.3) grows stronger and the plasma sheet becomes thinner. The stretching of the magnetotail causes the particle source regions in the tail map to lower ionospheric latitudes [Pulkkinen et al., 1991]. It also moves the transition region between the dipolar and tail-like field lines earthward driving the plasma sheet particles closer to the Earth to chaotic motion and to the loss cone [Sergeev et al., 1990]. These scenarios are suggested to explain the equatorward drift of the growth phase aurora.

The expansion phase takes over from a substorm onset when the usually most equatorward auroral arc intensifies and becomes dynamic evolving into multiple arcs and vortex-type structures [Voronkov et al., 2000]. Several brightenings can occur during the growth phase, but the expansion phase onset is the intensification that leads to the full-scale dynamics (the third row in Figure 4.1). During the expansion, the cross-tail current disrupts and diverts to the ionosphere forming a loop called Substorm

Current Wedge (SCW). The SCW current flows into the ionosphere on the eastward side of the loop as shown by Figure 4.3. The return flow to the magnetosphere is found in the western part of the loop. As a consequence of SCW, a negative deviation in the magnetic X-component is strongly intensified (see Figure 4.2). The auroral signature associated with the SCW and the disruption of the cross-tail current is a Westward Travelling Surge (WTS) [Akasofu et al., 1965] (the first image on the bottom row of Figure 4.1), which often looks much like a huge spiral form. Surge and spiral structures have similar sizes and the same winding direction. They both cause negative magnetic deflections on the ground and are related to the upward FACs [Davis and Hallinan, 1976; Opgenoorth et al., 1983]. However, the western edge of the WTS winds in the direction of the surrounding plasma flow, i.e. clockwise when viewed along the magnetic field [Nakamura et al., 1993]. The final structure, however, has a counterclockwise winding. Although a well-developed spiral has the same winding direction as a WTS, it evolves in the direction opposite to the plasma flow (PUBL. II). Thus, a WTS should not be considered as a large spiral.

The westward travelling surge corresponds to the western edge of the expanding bulge in the auroral oval. An example of the evolution of the auroral oval is shown by Figure 4.4. An auroral bulge forms from the breakup region of the oval expanding both poleward and along the oval. Other expansion phase signatures are, for example, launching of magnetic Pi2 pulsations[1] [Yumoto et al., 1989] that can be observed by both the ground-based and satellite-borne instruments, and particle injections at geosynchronous orbit [Reeves et al., 1990]. Dipolarisation of the magnetotail [Liou et al., 2002] returns the stretched tail field into a more dipolar-like configuration. This can be monitored from the ground-based recordings of the proton emission, since as a consequence of the plasma sheet thickening, the proton emission band moves poleward. The dipolarisation may also be related to a release of an island of closed magnetic field configuration, a plasmoid [Hones et al., 1984]. An example of a substorm expansion phase is described and analysed in PUBL. V.

During the recovery phase, the magnetosphere relaxes to the more dipolar configuration it had prior to the substorm [Opgenoorth et al., 1994]. The auroral electrojets decay as does the negative magnetic bay. The auroral oval often splits to form a double-oval [Elphinstone and Hearn, 1992]. The most intense aurora fades, but Greek Ω-shaped aurora (omega bands) [André and Baumjohann, 1982] as well as patchy and pulsating aurora [Johnstone, 1983] are typically seen in the morning sector during this phase.

Typically, the whole substorm sequence lasts for 2–3 hours. Although a general idea of what will happen in the aurora exists, individual substorms are often very different from each other. Many studies cover only a certain time period of the substorm, a certain magnetospheric or ionospheric part of the process or just one type of measurements. For example, the aurora shown by Figure 4.1 seemed to follow the typical

[1] Irregular pulsations with the period of 40–150 s and the frequency of 2–25 mHz.

substorm sequence, but the magnetometer recordings disagree. Figure 4.5 presents the variations in the magnetic X-component at the ASC station (KIL) for the time period of the auroral images in Figure 4.1. The moments when the ASC images were taken are marked by arrows. As compared to the average substorm behaviour in Figure 4.2, this looks very different. The magnetic recordings suggest that the brightening and the equatorward drifting arcs take place at the beginning of the expansion and the WTS-like structure occurs when the magnetic deflection is already recovering. This example event shows that it is important to collect substorm signatures from different types of data.

The substorm phases and the corresponding ionospheric phenomena are fairly well investigated, while their counter-processes in the magnetosphere as well as the relative timing of the different processes require further research. Answering these open questions is the main objective of the National Aeronautics and Space Administration's (NASA) Time History of Events and Macroscale Interactions during Substorms (THEMIS) project. A very dense ground-based imager network is being built to maximise the possibility of conjugate studies between the ground stations and five satellites, whose launch is in 2006. In the magnetotail, the orbits of the satellites will bracket the regions of the current disruption and reconnection in order to resolve their relative timing at the beginning of a substorm.

4.2 SMALL SUBSTORMS OR PSEUDO-BREAKUPS?

Auroral activity may start with signatures characteristic to a substorm growth phase, but then cease before reaching the full extent of the expansion phase. These activity periods are called pseudo-breakups. Despite the ionospheric and magnetospheric features similar to those of a substorm [Pulkkinen, 1996; Aikio et al., 1999], the pseudo-breakup related processes as the current disruption, substorm current wedge and dipolarisation appear as localised versions of the corresponding global-scale phenomena of the substorms. In addition to being localised, pseudo-breakups only last for a few tens of minutes. They often occur as precursors of the expansion phase during the substorm growth phase [Koskinen et al., 1993].

The conditions that prevent the pseudo-breakup activity from evolving into a full-scale substorm are not known for sure. Suggested reasons include too slow or too transient energy transfer from the solar wind to the magnetosphere, insufficient storage of energy in the magnetotail [Nakamura et al., 1994; Amm et al., 2001] and ionospheric conductivity, which is not high enough to close the substorm current wedge [Koskinen et al., 1993]. In the ionosphere, vortices are often observed as an auroral display of the pseudo-breakup activity. An event like this was studied in PUBL. III, which also discussed the differences between the ionospheric electrodynamics of the pseudo-breakups and the substorms. The event of interest showed that the currents were closed in the vicinity of the pseudo-breakup spirals, but the alignment of the current loop was

rather across the auroral oval than along it. An earlier study by Amm et al. [2001] analysed a pseudo-breakup occurring simultaneously with a substorm but westward of the main activity. In this case, the ionospheric current loop was oval-aligned like the ionospheric part of the SCW (see Figure 4.3) and the closing downward FAC region located outside of the MIRACLE FOV.

As shown by Kallio et al. [2000], the size of the substorm activity is closely related to the energy input from the solar wind to the magnetosphere at the dayside magnetopause. If the energy input ceases (the IMF B_Z turns northward) during the growth phase or near the onset time, as in the event studied in PUBL. III, the following substorm tends to be small. If, on the other hand, the energy is continuously transferred to the magnetosphere throughout the whole expansion phase, it is likely to cause stronger activity. A fact that makes the pseudo-breakup versus substorm discussion even more confusing is that there is no single straightforward definition for a pseudo-breakup, but it rather depends on the particular data set used in the analysis. As long as no unambiguous definition for a pseudo-breakup or a clear difference between a pseudo-breakup and a substorm is found, pseudo-breakup studies are important in addition to the studies on full-scale substorms.

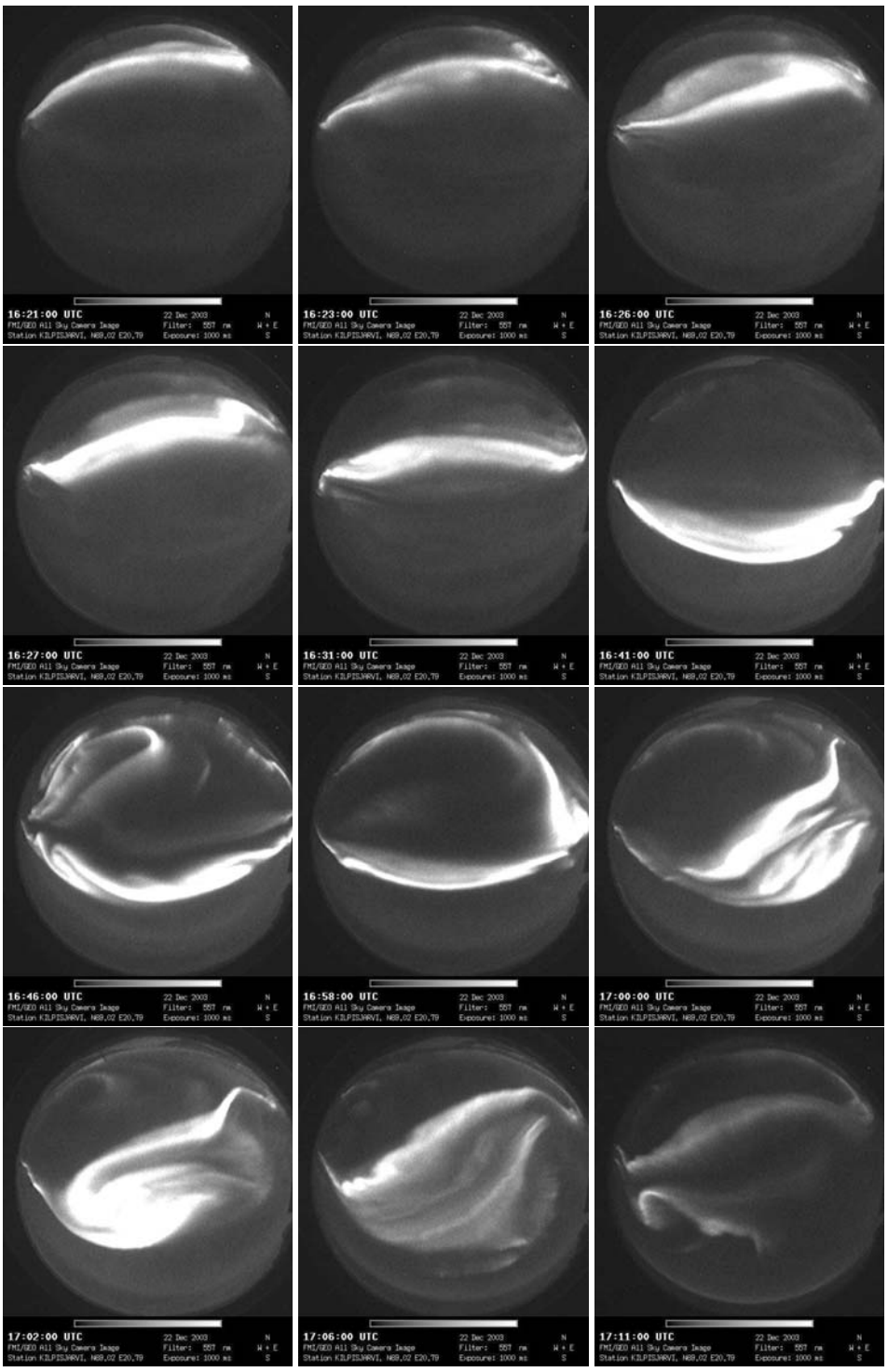

Figure 4.1. A series of ASC images taken at KIL station on 22 Dec 2003. The evolution of the aurora shows a substorm type activity. Equatorward drifting arc (two first rows), brightening leading to the breakup or an intensification of a breakup (third row), WTS (first image on the bottom row) and fading of the aurora (two last images). Note the irregular time interval between the images.

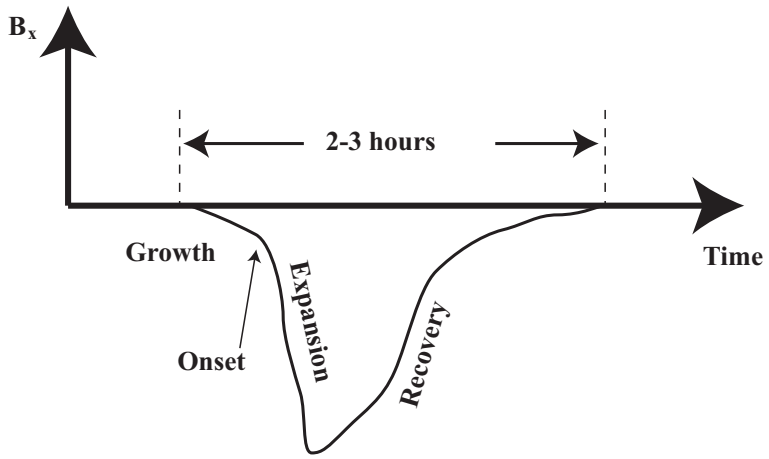

Figure 4.2. Average behaviour expected in the X-component of the ground-based magnetic field during a substorm. A typical time scale for an isolated substorm is 2–3 hours. Illustration by Mikko Syrjäsuo, after Kamide [1991].

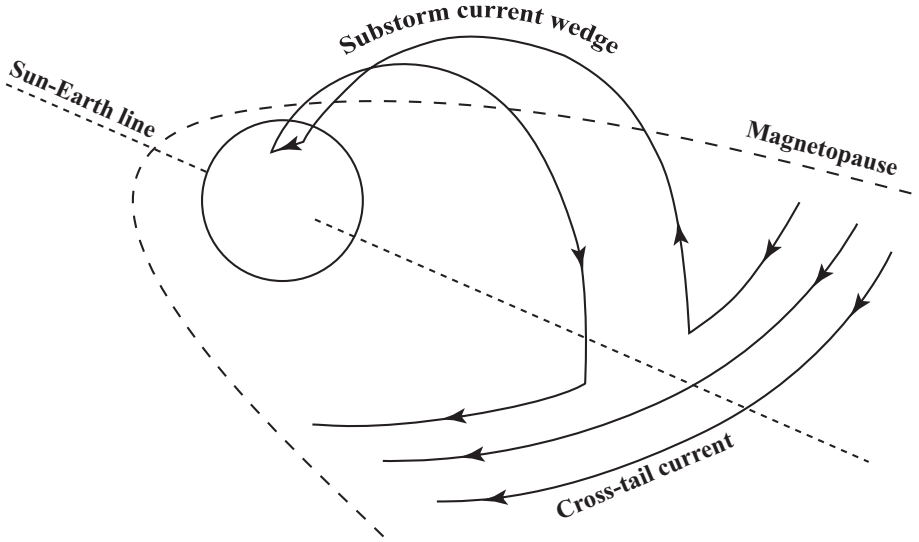

Figure 4.3. A schematic picture of a substorm current wedge. The current flowing across the magnetotail from dawn to dusk is partly closed by the ionospheric electrojet currents. Directions of the currents (arrows) are into the ionosphere on the eastern and out of the ionosphere on the western edge of the loop. Illustration by Mikko Syrjäsuo, after McPherron et al. [1973].

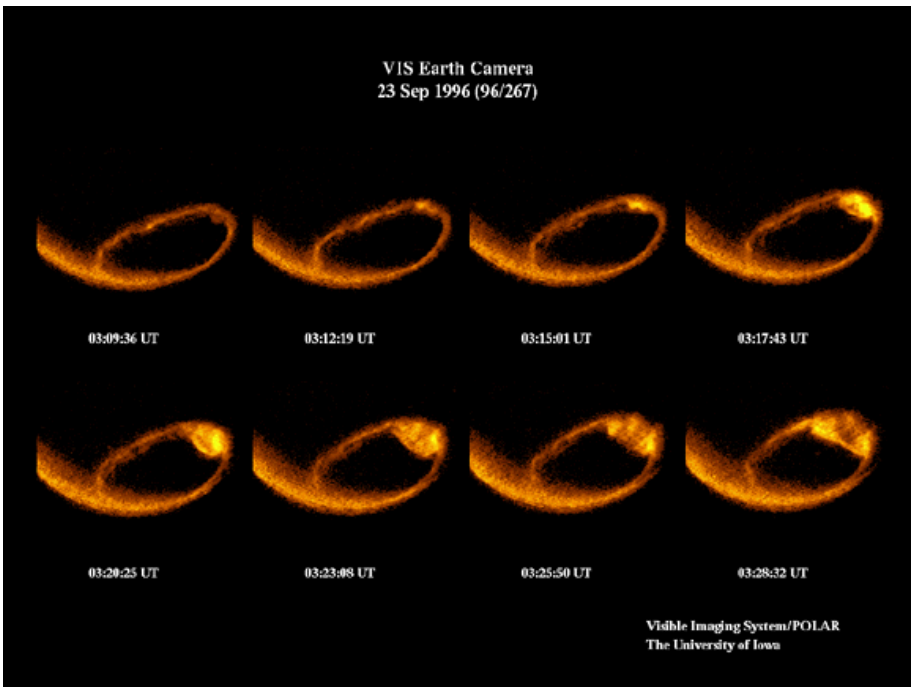

Figure 4.4. Expansion of a bulge in the auroral oval as seen by the UV imager on board the Polar satellite. Courtesy of Windows to the Universe, at http://www.windows.ucar.edu/

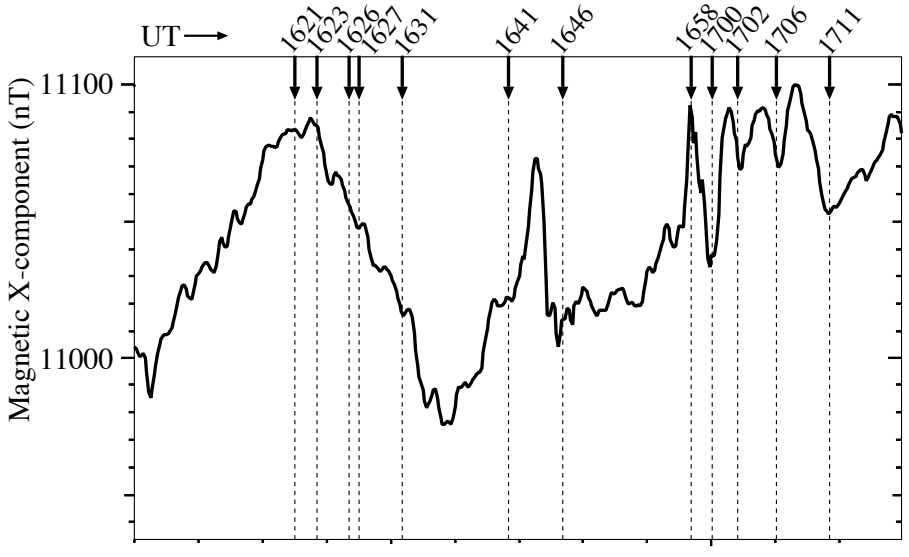

Figure 4.5. Variations of the magnetic X-component at the ASC station in Kilpisjärvi on 22 Dec 2003. The time period corresponds to the one in Figure 4.1 and the moments when the ASC images were taken are marked by arrows, dashed lines and corresponding UT times.

5 MODELS AND METHODS

5.1 SPIRAL MODEL BY HALLINAN

The model by Hallinan [1976] was the first theoretical attempt to explain spiral forms in the aurora. As an auroral arc is accompanied by an upward FAC sheet, this model states that the spiral formation arises from a shear (a localised enhancement) in the FAC. The enhanced FAC filament produces a magnetic field perpendicular to the current sheet, which then acts to bend the field lines as the disturbance propagates earthward. A spiral is formed in the ionospheric end of the FAC sheet while the initial perturbation in the magnetospheric end is small as illustrated by Figure 5.1. The mathematical

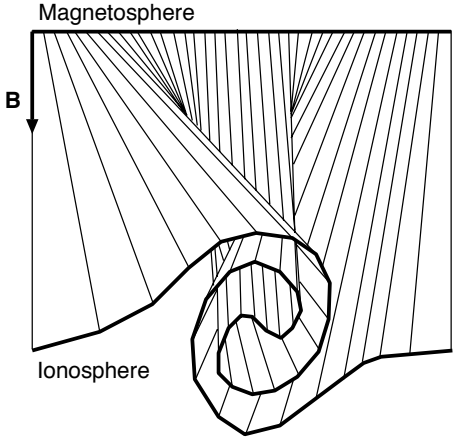

Figure 5.1. Spiral formation along the magnetic field line from a small perturbation in the magnetospheric end towards the ionosphere. Illustration by Mikko Syrjäsuo, after Davis [1978].

description of this phenomenon is rather simple, since a cartesian coordinate system (X is eastward, Z is northward and Y completes the right-handed system, see Figure 5.2) is used and the background magnetic field (B_{0Z}) is assumed to be a constant instead of, for example, a dipole field. Another part of the background magnetic field is the field due to the current sheet (B_{0X}). Both the background ($\mathbf{B_0}$) and the perturbation field ($\mathbf{B_1}$) caused by the enhancement in the sheet current obey the Ampère's law $\mu_0\mathbf{j} = \nabla \times \mathbf{B}$. The perturbation magnetic field is described by a plane wave approximation: $\mathbf{B_1} = Ae^{i\alpha X + i\gamma Z}$, where α and γ are the wave numbers along X and Z, respectively, and $A = A(Y)$ (detailed expressions are calculated in PUBL. II). Assuming a force balance equation of $\mathbf{j} \times \mathbf{B} = \nabla p$, where p is the thermal pressure, the calculations to solve the instability growth rate can be performed.

The details of the model are given in PUBL. II, where the growth rate of the FAC instability (i.e. the vertical wave number γ) is solved first to the extent of Hallinan [1976]. He assumed that the growth along the magnetic field is much stronger than the

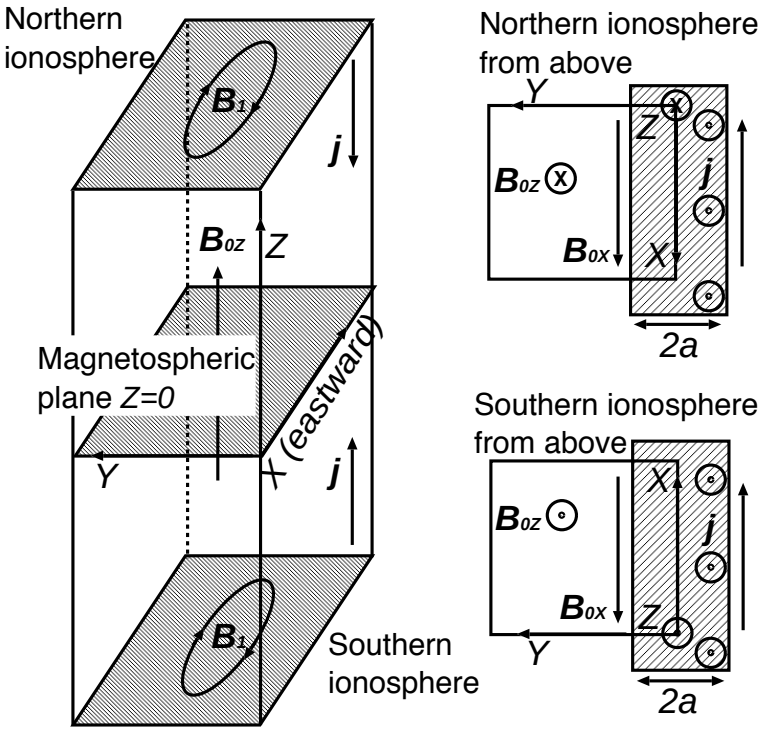

Figure 5.2. The spiral model by Hallinan [1976] is described in this cartesian coordinate system. Here, B_{0Z} is the vertical component of constant background magnetic field, **j** is the current density of the FAC sheet, B_{0X} is the horizontal part of the background field due to the current sheet, and $\mathbf{B_1}$ is the perturbation field caused by the FAC enhancement.

one in the horizontal direction ($\gamma \gg \alpha$) and obtained the following expression for the growth rate:

$$\gamma_H = \pm\sqrt{\frac{\mu_0^2 j^2}{4B_{0Z}^2}[(2ka-1)^2 - e^{-4ka}]} \tag{5.1}$$

where μ_0 is the vacuum permeability, j is the current density of the underlying FAC sheet, B_{0Z} is the vertical component of the background magnetic field, a is the half-width of the FAC sheet, and k holds the relation between the horizontal and vertical wave numbers α and γ ($k^2 = \alpha^2 + \gamma^2$). When the assumption $\gamma \gg \alpha$ is withdrawn, the new growth rate in a more general form becomes

$$\gamma = \pm\sqrt{\frac{B_{0Xa}^{*2} k^{*2}[(2k^*-1)^2 - e^{-4k^*}]}{B_{0Xa}^{*2}[(2k^*-1)^2 - e^{-4k^*}] + 4k^{*2}B_{0Z}^{*2}}} \tag{5.2}$$

where $B_{0Z}^* = B_{0Z}/B_{0Z} = 1$, $\mu_0 ja = B_{0Xa}$, $B_{0Xa}^* = B_{0Xa}/B_{0Z}$, and $k^* = ka$, i.e. all asterisks indicate normalisation with respect to either the vertical component of the background magnetic field (B_{0Z}) or the half-width of the underlying arc (a). This equation allows us to examine the dependence of the growth rate on the strength of

the horizontal background magnetic field (B_{0Xa} due to the current sheet) in addition to B_{0Z}.

A proper testing of the free parameters of the model showed that the strongest growth appears when the horizontal wave number ($\alpha^* = \alpha a$) equals 0.4 (as was also discovered by Hallinan [1976]). Stronger B^*_{0Xa} implies greater growth rate (γ).

Hallinan's model in the more general form predicts a correct winding direction for the spirals on both hemispheres (PUBL. II). However, further evaluation of the model is difficult, since all the lengths and fields are scaled to the background magnetic field or to the half-width of the current sheet. Since the background field in the model is constant also the FAC sheet width remains the same. In reality, the arc widths are very different in the ionosphere and the magnetosphere, and their relation is determined by the geomagnetic field topology [Borovsky, 1993]. Thus, assumptions of the constant magnetic field and the constant width of the underlying auroral arc were good for the testing of the model but are not realistic. Further challenges in the model development would be to derive the model equations with e.g. a dipole background magnetic field, and also not to neglect the second harmonic terms of the pressure and the perturbation magnetic field, as it is done in PUBL. II.

5.2 ASCINV: AN INVERSION METHOD FOR ASC IMAGES

An inversion method for ASC images named ASCinv [Janhunen, 2001] has been tested in PUBL. IV. This method is designed for solving the problem $\mathbf{m} = \mathbf{A}\mathbf{u}$, where $\mathbf{u}$ is a vector of the unknowns (electron differential number fluxes), $\mathbf{m}$ is a vector containing the measurements (ASC images), and the matrix $\mathbf{A}$ describes the relation between the measurements and the unknowns. The electron differential number fluxes ($\mathbf{u}$) are calculated from a set of digital auroral images ($\mathbf{m}$) by minimising the difference $(\mathbf{A}\mathbf{u} - \mathbf{m})^2$ in an iterative way. The so called theory matrix $\mathbf{A} = \mathbf{G}\mathbf{P}$ contains information on both the imaging geometry $\mathbf{G}$ (e.g. direction of the true north and the tilt of the camera from vertical) and the emission physics $\mathbf{P}$. A detailed description of the content of the physics matrix is given in PUBL. IV and thus, this section concentrates on clarifying the difference between the original set up of the emission physics equations [Rees, 1963, 1989] and the upgraded version by Sergienko and Ivanov [1993]. The upgraded inversion is based on newer modelling work and in the test runs it provided results that were clearly more consistent with the low-altitude satellite measurements of the particle precipitation.

The physics matrix equations that are different in the original and upgraded version of ASCinv include electron range (R), energy distribution function of an isotropic source (Λ), excitation efficiency of blue (427.8 nm) photons (V_{428}) and ratios of volume emission rate profiles for the green (557.7 nm) and blue emissions (e_{g2b}) as well as for the red (630.0 nm) and blue emissions (e_{r2b}). These parameters are not described by analytically derived equations but rather by semi-empirical formulae. Equations for

emission rate ratio profiles are manually fitted to the model results by Sergienko and Ivanov [1993] in the improved method, and to the model output by Rees [1963, 1989] in the original ASCinv package. The model, on which the upgraded version is based, covers an energy range of 0.1–10 keV. It assumes monoenergetic initial fluxes, and the calculations also consider the strength of the magnetic dipole field in solving the ion production rate profiles stimulated by the electron precipitation.

One of the key parameters of the emission physics, the energy deposition rate (in keV/m^{3}s), is determined by the integral

$$\varepsilon(h) = \int dEF(E)\frac{\Lambda nE}{R} \tag{5.3}$$

where F is the electron differential number flux, n is the neutral atmospheric mass density and Λ and R are the energy distribution function of an isotropic source and the electron range, respectively.

The electron range is a function of particle energy (E in keV) and describes the effective distance from the source, at which an electron with the initial energy E stops. Like the atmospheric depth, this parameter corresponds to the column mass density of the medium integrated over the particle trajectory. In the model by Sergienko and Ivanov [1993], the electron source is set to the altitude of 700 km. The original range by Rees [1963] is based on laboratory measurements of the luminosity produced by a monoenergetic electron beam in a nitrogen gas and it is valid for an energy range of 0.2–50 keV. The expressions for the electron range in both the original and the upgraded ASCinv setup are ($\mathrm{kg/m^2}$)

$$R(E) = 4.30 \cdot 10^{-6} + 5.36 \cdot 10^{-5}E^{1.67} \qquad \text{and} \tag{5.4}$$

$$R_S(E) = 1.64 \cdot 10^{-5}E^{1.67}[1 + 9.48 \cdot 10^{-2}E^{-1.57}] \tag{5.5}$$

where energy is expressed in keV. Increase in these ranges as a function of the initial energy (0.2–50 keV) is shown in Figure 5.3. As the figure shows R is greater than R_S by roughly a factor of π. Thus, according to the emission physics of the original ASCinv, an electron with a certain energy E can reach greater effective distances from the source before stopping.

The energy distribution function $\Lambda(R)$ is a dimensionless normalised polynomial describing how the electron energy is dissipated along its range. It can be expressed by the following equation.

$$\Lambda(R) = \frac{dE}{E}/\frac{dz}{R} \tag{5.6}$$

where dE is the amount of energy deposited within the distance dz. In Figure 5.4 the energy distribution functions are plotted for the original and the upgraded ($\Lambda_S(R_S)$) ASCinv versions. Both distributions peak at the lower part of the electron range, but the upgraded one spreads out more towards the higher energies. For small ranges (and low particle energies), the energy dissipation according to the newer modelling by Sergienko and Ivanov [1993] is much less efficient.

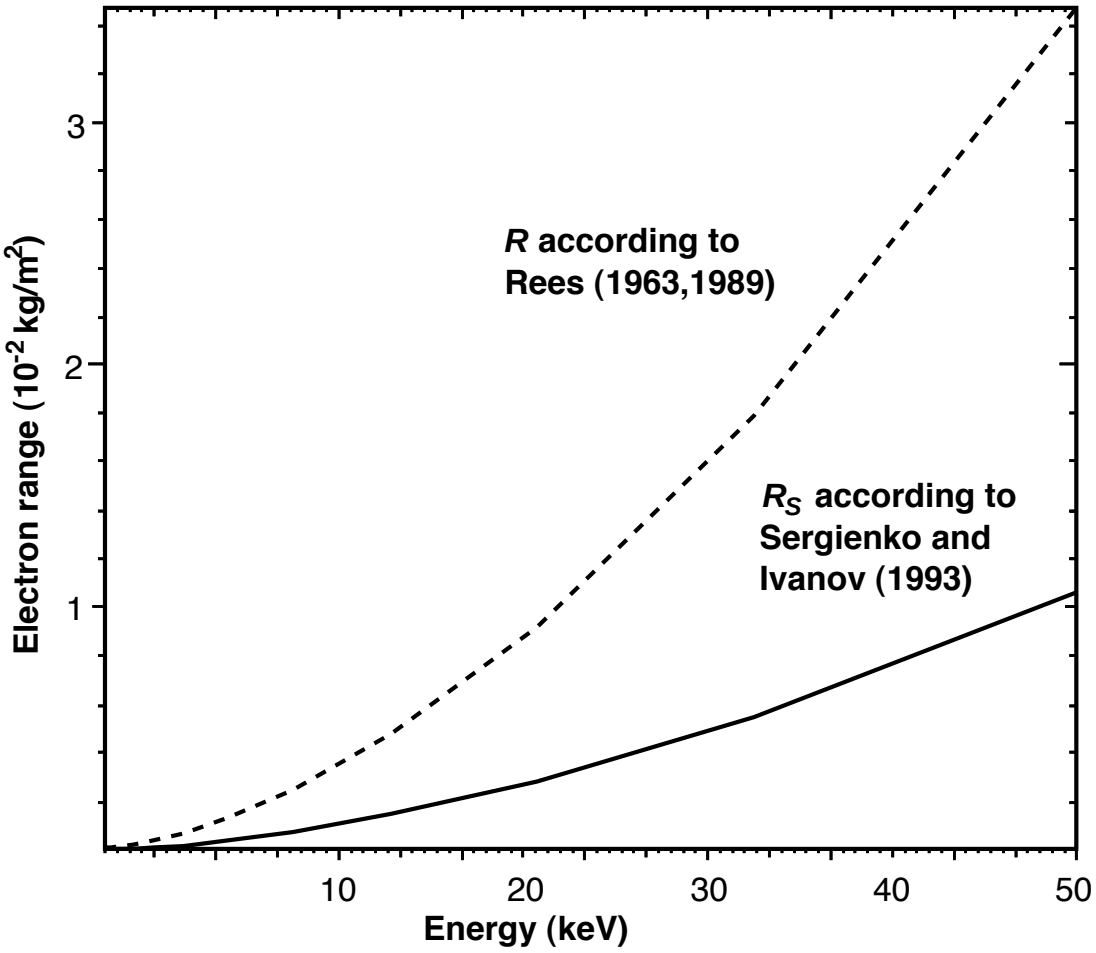

Figure 5.3. Electron ranges by Rees [1963, 1989] (dashed line, R) and Sergienko and Ivanov [1993] (solid line, R_S). According to the newer model, the range is smaller by a factor of π for all energies.

The original physics matrix assumes a constant yield of blue photons of about 160 R per 1 $\mathrm{mW/m^2}$. According to Rees and Luckey [1974], the yield depends on the characteristic energy of the electron precipitation. The value used by ASCinv corresponds to the energies of 1–2 keV and the estimated errors for higher energies are about 25% [Janhunen, 2001]. From a definition of a Rayleigh (1 R = 10^{10} photons/$\mathrm{m^2s}$), 160 R corresponds to $1.6{\cdot}10^{12}$ $\mathrm{photons/m^2s}$. On the other hand, 1 $\mathrm{mW/m^2}$ equals $6.24{\cdot}10^{12}$ $\mathrm{keV/m^2s}$. Consequently, the excitation efficiency becomes a constant:

$$V_{428} = 0.256 \frac{\mathrm{photons}}{\mathrm{keV}} \tag{5.7}$$

In the upgraded version, an altitude dependence is introduced by the number densities of the main atmospheric constituents (nitrogen and oxygen) at the auroral altitudes. This gives an efficiency of

$$V_{S428} = \frac{n_{\mathrm{N_2}}(h)}{n_{\mathrm{N_2}}(h) + 0.7 n_{\mathrm{O_2}}(h) + 0.4 n_{\mathrm{O}}(h)} \cdot 0.628 \ \mathrm{photons/keV}, \tag{5.8}$$

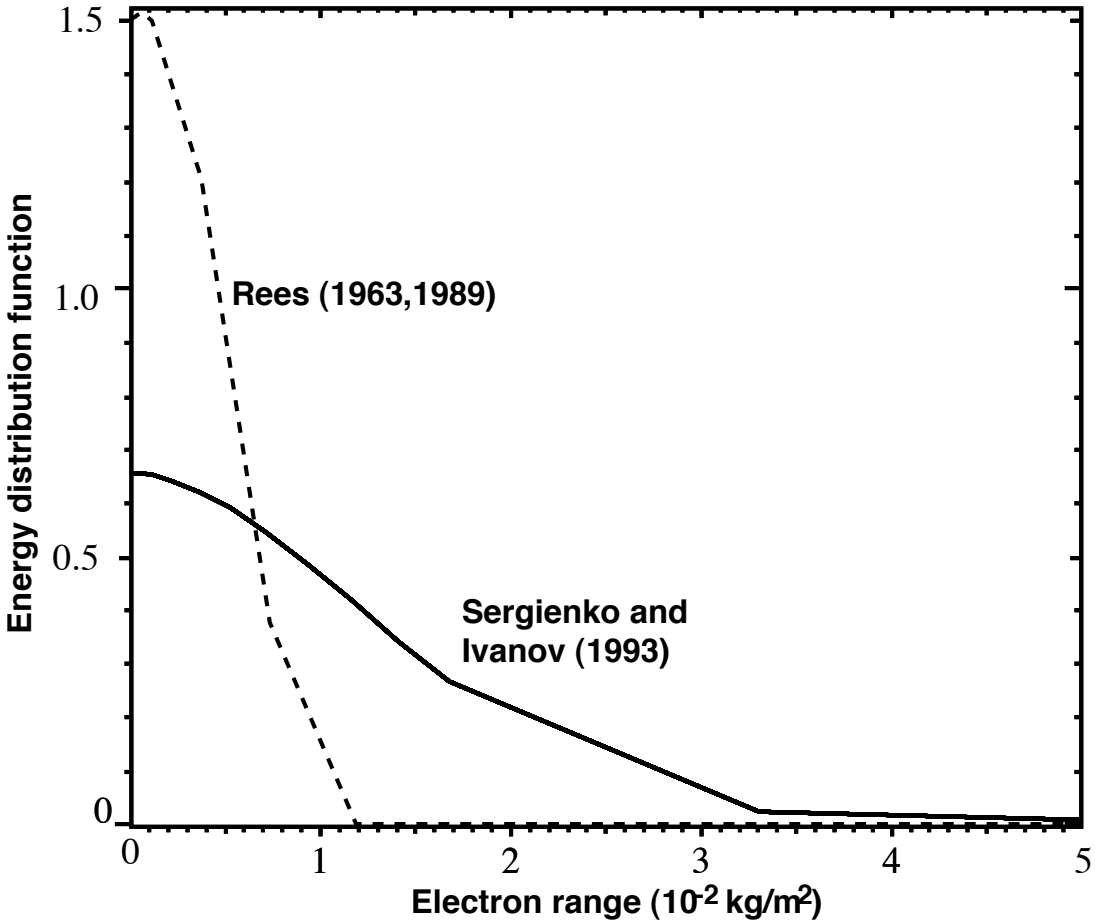

Figure 5.4. Energy distribution functions by Rees [1963, 1989] (dashed line, Λ) and Sergienko and Ivanov [1993] (solid line, Λ_S) as a function of electron range. The modified distribution spreads out more evenly along the range.

where h refers to the altitude and the number densities of nitrogen (n_{N_2}) and oxygen (n_{O_2} and n_{O}) are obtained from the model atmosphere called MSIS-86 thermospheric model [Hedin, 1987]. Using the typical ionospheric density values of these constituents, the factor of number densities is less than one, and the upgraded yield of blue photon varies around 200 $\mathrm{R}/(\mathrm{mW}/\mathrm{m}^2)$.

When the above explained modifications are applied, the resulting ratios of the emission rate profiles of different wavelengths e_{g2b} and e_{r2b} change as well. This follows from the fact that the energy deposition rate (ε) multiplied by the excitation efficiency (V_{428}) gives the emission rate profile for the blue photons, from which the other emission rate profiles are derived. Figures 5.5 and 5.6 show the modified emission rate ratio profiles as compared to the ones of the original inversion. The green-to-blue emission rate ratio (Figure 5.5) by Sergienko and Ivanov [1993] varies around a value of five at the altitudes from 110 km to 200 km, while the original profile by Rees and Luckey [1974] increases monotonically between 2–13. Both ratio profiles of the red-to-blue

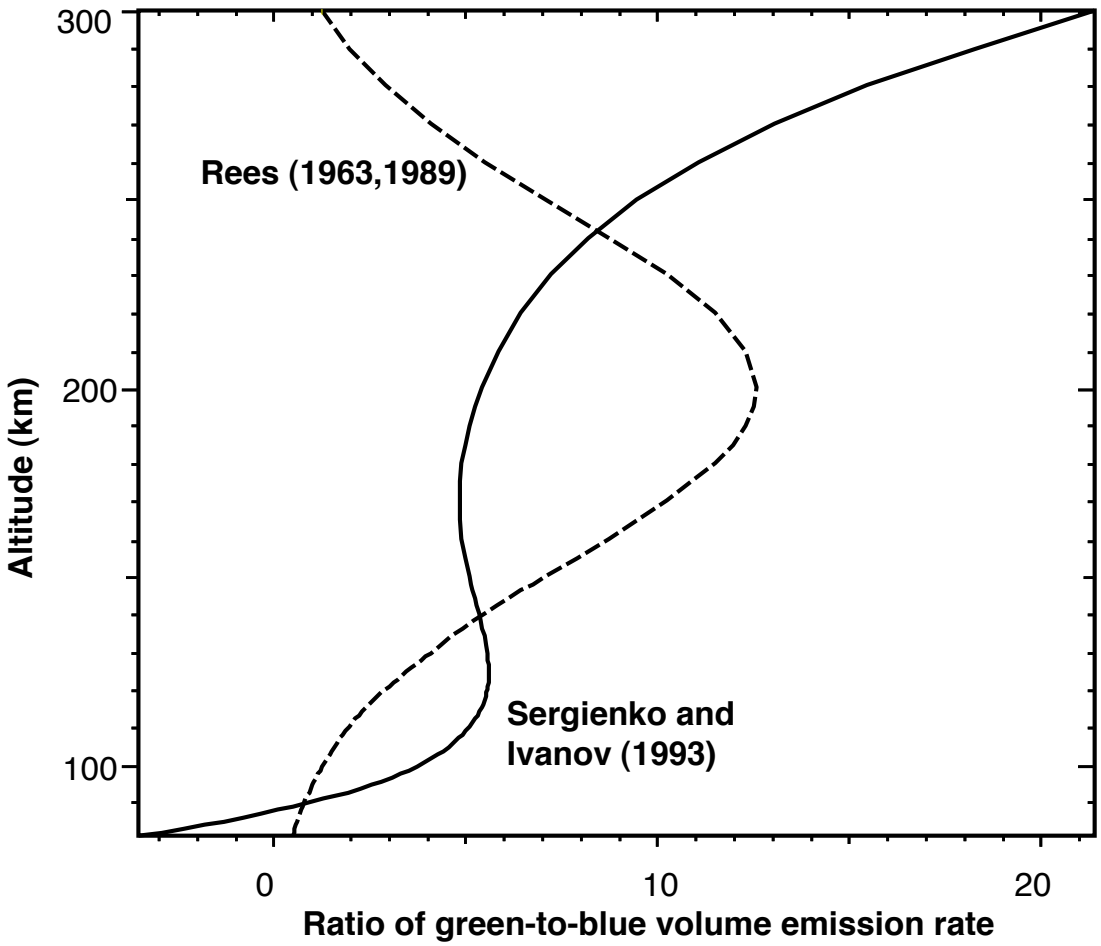

Figure 5.5. Ratio profile of the green-to-blue emission rate e_{g2b} according to modifications by Sergienko and Ivanov [1993] (solid line) compared to the one by Rees [1963, 1989] (dashed line). The local maximum of the emission rate is changed from 200 km (dashed line) down to about 110 km (solid line). Above 250 km the difference between the models becomes larger.

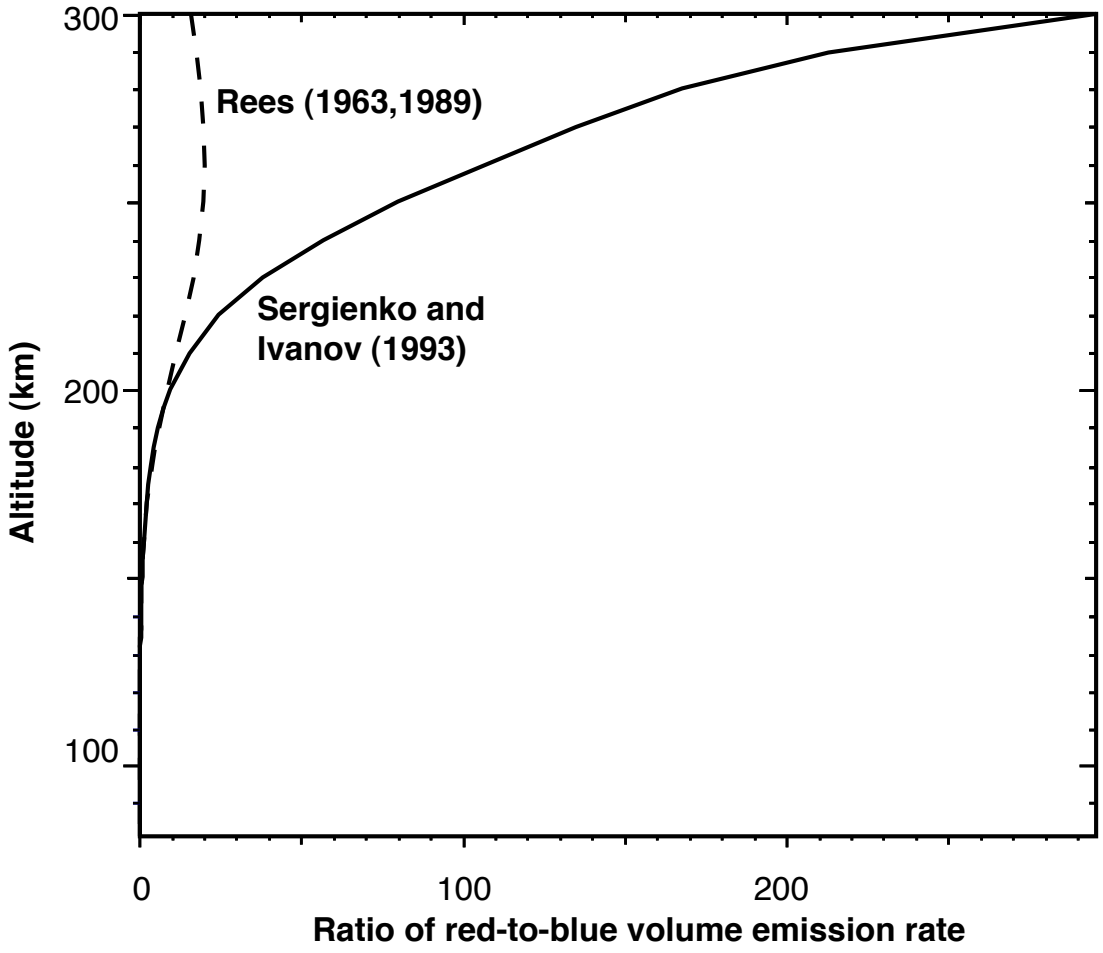

Figure 5.6. Ratio profile of the red-to-blue emission rate $e_{r\text{-}2b}$ according to modifications by Sergienko and Ivanov [1993] (solid line) compared to the one by Rees [1963, 1989] (dashed line). Up to the altitude of 200 km the behaviour of these curves is very similar.

emission rate (Figure 5.6) behave very similarly at the altitudes lower than 210 km. This is where most of the green and blue auroral emission originates, and only these two emission lines have been used as an input in testing the ASCinv programme.

As concluded in PUBL. IV the upgraded inversion programme produces smaller electron energy flux values than the original one due to the above described changes in the emission physics equations according to more recent modelling work. The upgraded inversion results are also clearly in a better agreement with the satellite measurements of energy fluxes.

5.3 OTHER METHODS

5.3.1 Spectrum: An inversion method for EISCAT data

Spectrum inversion [Kirkwood, 1988] solves electron energy characteristics from altitude profiles of electron density measured by the EISCAT radars. The method is described in more detail in PUBL. IV. As the input Spectrum reads field-aligned electron density profiles. It uses the MSISE-90 (Neutral Atmosphere Empirical Model from the surface of the Earth to the lower exosphere) statistical model atmosphere [Hedin, 1991] to determine neutral atmospheric parameters, such as neutral density, atmospheric depth (a line-integral of the mass density of the overlying air), neutral temperature, ion-neutral and electron-neutral collision frequencies as well as number densities of different atmospheric constituents (e.g. O_2, O^+ and N_2). With this information, the Spectrum programme inverts the average energy of the precipitating particles, their differential number and energy fluxes, and an estimate of the field-aligned current. Furthermore, the ionospheric conductivities can be calculated by using the following equations [Krall and Trivelpiece, 1973]:

$$\sigma_H(h) = \frac{n_e q}{B}\left[\frac{\omega_e^2}{\nu_{en}^2 + \omega_e^2} - \frac{\omega_i^2}{\nu_{in}^2 + \omega_i^2}\right] \tag{5.9}$$

$$\sigma_P(h) = \frac{n_e q}{B}\left[\frac{\omega_i \nu_{in}}{\nu_{in}^2 + \omega_i^2} + \frac{\omega_e \nu_{en}}{\nu_{en}^2 + \omega_e^2}\right] \tag{5.10}$$

where q is the electron charge, n_e is the number density of charged particles, B is the background magnetic field strength, ω_e and ω_i are the electron and ion gyrofrequencies, respectively, and ν_{in} and ν_{en} are the ion-neutral and electron-neutral collision frequencies, respectively. Again, the collision frequencies are taken from the MSISE model atmosphere. The value for B is taken as $5.5 \cdot 10^{-5}$ T. The assumption for ω_i is 160 s^{-1} and 177 s^{-1} for the altitudes below and above 150 km, respectively, while ω_e is $8.8 \cdot 10^6$ s^{-1}.

Because the input electron density profiles are point measurements, the output precipitation characteristics correspond to single points as well. Thus, the spatial resolution, as defined by the radar beam width, is high (1–3 km at the ionospheric altitudes).

The temporal resolution of the post-integrated radar data is typically 128 seconds, because the weak backscatter often requires a fairly long post-integration time in order to enhance the signal-to-noise ratio. The calculation of the total electron energy flux uses differential number fluxes of particles with energies above 3 keV. This is because below this energy limit, the uncertainties of the Spectrum results increase [Kirkwood, 1988]. As the energies related to a typical auroral arc range from about 1 keV on, the lower energy limit of the energy flux integral is rather high, which should be kept in mind when interpreting the Spectrum results.

This method has been used to study, for instance, changes in the precipitating electron energy characteristics of evolving aurora such as the breakup aurora [Kirkwood and Osepian, 1995]. In this thesis, we used electron energy fluxes from Spectrum as a reference data set to the inverted energy fluxes from ASCinv (see PUBL. IV). Although this comparison involved two different types of indirect measurements with very different spatial and temporal resolution, the resulting energy fluxes were typically of the same order of magnitude.

5.3.2 Method of Characteristics

The Method of Characteristics, originally introduced by Inhester et al. [1992], is designed for solving ionospheric electrodynamics from the ground-based measurements. In this method the ionosphere is modelled as an infinitely thin conducting layer perpendicular to the magnetic field lines at the altitude of 100 km. Above the ionosphere, the horizontal conductivities vanish and the field-aligned conductivity approaches infinity. Zero conductivities are assumed below the ionosphere. The effect of the neutral winds is not taken into account, and the numerical solution is performed in cartesian coordinate system.

An improved version of the method [Amm, 1995] has been applied to MIRACLE data to determine the horizontal and field-aligned currents and the horizontal distribution of height-integrated Hall and Pedersen conductivities. The method is based on the following equations: 1) The ionospheric Ohm's law

$$\mathbf{J} = \Sigma_P \mathbf{E} + \Sigma_H (\hat{\mathbf{b}} \times \mathbf{E}) \tag{5.11}$$

where $\mathbf{J}$ is the horizontal height-integrated ionospheric current,Σ_P is the Pedersen conductance, Σ_H is the Hall conductance, $\hat{\mathbf{b}}$ is the unit vector along the magnetic field, and $\mathbf{E}$ is the ionospheric electric field. 2) The current continuity in the ionospheric plane

$$\mathbf{j} = \nabla_h \cdot \mathbf{J} \tag{5.12}$$

where $\mathbf{j}$ is the FAC density and the subscript h refers to the horizontal part of the operator. 3) An assumption that immediately below the ionospheric plane the horizontal part of the external magnetic field ($\mathbf{B_{Ion,h}}$) is related to the divergence-free part of the total horizontal current ($\mathbf{J_{df}}$)

$$\mathbf{B_{Ion,h}} = -\frac{\mu_0}{2}(\hat{\mathbf{z}} \times \mathbf{J_{df}}) \tag{5.13}$$

where $\hat{\mathbf{z}}$ is a unit vector perpendicular to the ionospheric plane and earthward and μ_0 is the vacuum permeability. From these constraints, the partial differential equation to be solved becomes

$$\mathbf{W} \cdot (\nabla_h \Sigma_H) + (\nabla_h \cdot \mathbf{W}) \Sigma_H = \frac{2}{\mu_0} \nabla_h \cdot \mathbf{B_{Ion,h}} \tag{5.14}$$

where $\mathbf{W}$ is related to the measured ionospheric electric field $\mathbf{E_M}$ by the equation $\mathbf{W} = \mathbf{E_M} - \xi^{-1} \hat{\mathbf{z}} \times \mathbf{E_M}$, where $\xi = \Sigma_H / \Sigma_P$. Measured electric field ($\mathbf{E_M}$) is then used to replace the above ionospheric field $\mathbf{E}$.

The above equation does not contain an assumption of the electrostatic potential field ($\nabla_h \times \mathbf{E} \neq \mathbf{0}$). The solution of this two-dimensional differential equation includes splitting it into one-dimensional differential equations as described by Amm [1995].

The input data for the Method of Characteristics are an estimate of the Hall-to-Pedersen conductance ratio (ξ), electric field measurements ($\mathbf{E_M}$) from the STARE radar and the upward continued horizontal magnetic field deflections from IMAGE data. The upward continuation [Amm and Viljanen, 1999] makes the magnetic field recordings from the ground describe the magnetic field variations immediately below the ionospheric level. The technique uses superposition of ionospheric divergence-free elementary current systems to reproduce the magnetic field variations measured on the ground. When the ionospheric current system has been modelled, the corresponding magnetic deflections can be calculated at the ionospheric altitudes. Thus, the upward continued magnetic field data are directly supplementary to other ionospheric measurements unlike the ground magnetic recordings, which can only be used to qualitatively estimate the magnetic deflections in the ionosphere. The input parameters have to be specified in every grid point of the two-dimensional model region. The conductance ratio is a user-defined parameter and its typical values vary from one to three. Auroral images can be used when choosing ξ so that lower values correspond to the regions outside the aurora and higher values to the regions of the auroral precipitation. However, the output of the method is not highly sensitive to the choice of the conductance ratio [Amm, 1995]. The spatial resolution of the method depends on the spacing of the magnetic measurements and is usually about 50 km being just enough for meso-scale auroral studies. The relatively high time resolution of 20 s of the input observations makes it possible to apply the method also to the studies of more transient auroral forms. Within these resolution limits, the method has proved to be reliable [Amm, 1995], and it has also been modified to work in the spherical coordinate system [Amm, 1998].

This thesis utilises the Method of Characteristics in an event study of ionospheric currents in the vicinity of a pseudo-breakup spiral as described in PUBL. III.

CONCLUSIONS AND FUTURE VIEWS

This thesis demonstrates different methods to derive physics out of the ground-based measurements of the aurora. The main instrument is the MIRACLE all-sky camera, and the publications I–V show how the digital all-sky camera data can be used in various ways. Even larger imager arrays, such as the ground-based geospace monitoring system supporting the THEMIS mission, will be built in the future with new challenges both spatially and temporally. Not only the methods introduced in this thesis, but all available data handling tools will then be highly important to make proper usage of the enormous amount of images.

In PUBL. I statistical analysis is used for learning about the average appearance of the auroral spiral forms. An important outcome is that the spirals are surprisingly common features and most of them are not related to high magnetic activity and do not necessarily imply magnetospheric conditions unstable for a ballooning or other more global instability. In PUBL. II, the auroral images from both hemispheres confirm that the prediction of the mathematical model is correct for the spiral winding. PUBL. III and PUBL. V are case studies where the all-sky camera data provide the core of the ground-based observations, but are supported by other measurements to build a picture of the event of interest as complete as possible. PUBL. III brings the auroral spiral into the context of intermediate activity, a pseudo-breakup, investigating its electrodynamics, especially the field-aligned current closure in the spiral vicinity. PUBL. IV utilises intensity calibrated auroral images as an input to an inversion programme, which then turns the brightness values into physical parameters, i.e. electron energy fluxes. Finally, PUBL. V shows the inverted electron energy fluxes of a spiral pair in the middle of a full-scale substorm sequence.

The numerical spiral model presented in PUBL. II raises many questions for the future work. It would need a more realistic background magnetic field, for example, a dipole field instead of the constant one. This way, it would be possible to estimate the strength of the FAC enhancement needed for a spiral formation and to evaluate the spiral winding distance. Another limitation of the model is an assumption of a steady-state situation. It would be important to include the time-dependency since the information on the spiral winding is transferred by shear Alfvén waves, and the winding time (of the order of a minute) is comparable to the Alfvén transit time between the ionosphere and the equator in the magnetopshere. To bring the model closer to the real measurements would help in learning more about the mechanism of spiral formation as well as the conditions required.

The ASC inversion method includes some uncertainties, most of which are discussed in PUBL. IV and will not be repeated here. A quite recently discovered error source is that the blue emission band is not completely measured by the MIRACLE ASCs. The width of the bandpass filters is 3–4 nm, while the whole blue emission band is 5–6 nm wide and contains a side peak, which in certain conditions can have a mea-

surable contribution to the total brightness of the blue aurora. The model calculations by Sergienko and Ivanov [1993] assume that the whole bandwidth of this emission is recorded. On the other hand, they do not take into account the absorption and scattering of the blue emission by ozone and aerosols. Especially for the blue emission with the short wavelength the atmospheric attenuation is significant but rather difficult to estimate. The original inversion includes table values of a simple model by Oikarinen [2001] for the ozone absorption and Rayleigh scattering as well as an estimate of the scattering and absorption by aerosols. The problems with the bandwidth and the atmospheric effects of the blue emission, although not yet studied, are likely to affect the opposite way to the inverted energy fluxes. Further studies are necessary to judge to what extent these two effects cancel each other. The very good agreement between the inverted and measured energy fluxes encourages us to continue the development and testing of the inversion method. The goal is to obtain a tool that could be used in statistical inversion analyses of different auroral forms or different types of activity to show the average behaviour of the precipitating electron energy flux in different conditions.

The Spectrum inversion programme used for the EISCAT radar data is also worth a more extensive and systematic use. Several different versions of this programme as well as different programmes to solve the same inversion of the electron density profiles exist. At least a theoretical comparison between some of these different codes should be done. It would be important to find out if it is possible to extend the energy range to cover the precipitating particle energies also below the current lower limit of 3 keV while still keeping the errors in the results reasonably small. Furthermore, recently developed and tested EISCAT experiments may provide data with high time resolution (even less than a second) for more accurate inversion analysis.

SUMMARY OF THE PUBLICATIONS

PUBL. I: **Statistical study of auroral spirals**
This paper contains a statistical analysis of spiral forms in the aurora. The data set includes all-sky camera images of about 200 spiral events from the winters 1997–1999. The main parameters of interest were the size of the spirals, their lifetime, Magnetic Local Time (MLT), drift direction and their relation to the local geomagnetic activity. For the first time, this kind of a large set of spiral images was analysed and the winding direction was confirmed as for the Northern hemispheric observations. We also found out that the spiral forms are fairly common in all MLT sectors, and a surprisingly large amount of them is not related to substorm type magnetic activity.

PUBL. II: **On the winding of auroral spirals: Interhemispheric observations and Hallinan's theory revisited**
This publication presents the well-known spiral model by Hallinan [1976] in a more general form. This model predicts the winding direction of the spirals, which is verified by the all-sky auroral images from both hemispheres. As a new result, the generalised model provides a relation between the instability growth rate and the strength of the horizontal background magnetic field due to the FAC sheet. Our observations showed that the FAC associated to the spiral form increases when the spiral winds and decreases with an unwinding structure. This finding is consistent with the model. M. Freeman performed the analytical calculations of the model and its programming.

PUBL. III: **A pseudo-breakup observation: Localized current wedge across the post-midnight auroral oval**
A more detailed study of the electrodynamics in the surroundings of an auroral spiral is reported in this third paper. This is a case study where the spiral forms in the MIRACLE field-of-view at the time of a pseudo-breakup. Good ground-based data coverage allows us to use more advanced data analysis methods and thus, to discuss in detail the electric fields and currents related to the vortex. The overall activity within the auroral oval, near-Earth magnetosphere and the solar wind conditions are also reviewed. The decrease in the solar wind energy input at the pseudo-breakup onset time, as well as the unfavourable location of the activity region in the morning side of the Harang discontinuity were probably responsible for the activity to cease before a full-scale substorm expansion was reached. An important result is also the picture of the spiral current system, which closes in the vicinity of the vortex structure and whose direction was tilted from the east-west alignment of the oval.

PUBL. IV: **Testing an inversion method for all-sky images**
This study describes a recently developed inversion method for all-sky camera images and defines the accuracy and reliability of the inversion. The method uses the ASC images as an input and converts the brightness values to the precipitating electron energy fluxes. We tested its reliability by comparing the inverted energy fluxes to the cor-

responding measurements by the DMSP satellites and the EISCAT incoherent scatter radar on Svalbard. As a conclusion, the inversion method produces energy fluxes with the relative errors of only a few tens of percents. The best results are obtained when images of the blue emission are used, the area of interest is close to the zenith and the option for the emission physics upgrade by Sergienko and Ivanov [1993] is added. This kind of proper testing is the first step towards the quantitative usage of the ASC images.

PUBL. V: **An inversion method for all-sky images: A substorm study**
This paper presents similar testing as PUBL. IV but for a different imaging system: a CANOPUS camera in Gillam, Northern-Canada. This shows that the inversion method is valid regardless of the imaging system. In addition to the promising testing results, the first time series analysis with this method was discussed showing how the precipitating electron energy flux varies during an auroral substorm. Together with other complementing instruments, such as riometers, the inversion appeared to be a promising tool for studies on the substorm energetics.

REFERENCES

Aikio, A., Opgenoorth, H., Persson, M., and Kaila, K., Ground-based measurements of an arc-associated electric field, *Journal of Atmospheric and Terrestrial Physics*, *55*, 797–808, 1993.

Aikio, A., Sergeev, V., Shukhtina, M., Vagina, L., Angelopoulos, V., and Reeves, G., Characteristics of pseudobreakups and substorms observed in the ionosphere, at the geosynchronous orbit, and in the midtail, *Journal of Geophysical Research*, *104*, 12263–12287, 1999.

Aikio, A., Lakkala, T., Kozlovsky, A., and Williams, P., Electric fields and currents of stable drifting auroral arcs in the evening sector, *Journal of Geophysical Research*, *107*, SIA 3–1, 2002.

Akasofu, S.-I., The development of the auroral substorm, *Planetary and Space Science*, *12*, 273–282, 1964.

Akasofu, S.-I., Kimball, D., and Meng, C.-I., Dynamics of the aurora, II, Westward traveling surges, *Journal of Atmospheric and Terrestrial Physics*, *27*, 173, 1965.

Aksnes, A., Amm, O., Stadsnes, J., Østgaard, N., Germany, G., Vondrak, R., and Sillanpää, I., Ionospheric conductances derived from satellite measurements of auroral UV and X-ray emissions, and ground-based data: A comparison, *submitted to Annales Geophysicae*, 2004.

Amm, O., Direct determination of the local ionospheric Hall conductance distribution from two-dimensional electric and magnetic field data: Application of the method using models of typical ionospheric electrodynamic situations, *Journal of Geophysical Research*, *100*, 21473–21488, 1995.

Amm, O., Method of characteristics in spherical geometry applied to a Harang discontinuity situation, *Annales Geophysicae*, *16*, 413–424, 1998.

Amm, O. and Viljanen, A., Ionospheric disturbance magnetic field continuation from the ground to the ionosphere using spherical elementary current systems, *Earth Planets Space*, *51*, 431–440, 1999.

Amm, O., Janhunen, P., Opgenoorth, H., Pulkkinen, T., and Viljanen, A., Ionospheric shear flow situations observed by the MIRACLE network, and the concept of Harang discontinuity, in *Magnetospheric current systems*, edited by S.-I. Ohtani, R. Fujii, M. Hesse, and R. Lysak, vol. 118 of *Geophysical Monograph Series*, pp. 227–236, AGU, 2000.

Amm, O., Janhunen, P., Kauristie, K., Opgenoorth, H., Pulkkinen, T., and Viljanen, A., Mesoscale ionospheric electrodynamics observed with the MIRACLE network: 1.

Analysis of a pseudobreakup spiral, *Journal of Geophysical Research*, *106*, 24675–24690, 2001.

André, D. and Baumjohann, W., Joint two-dimensional observations of ground magnetic and ionospheric electric fields associated with auroral currents 5. Current system associated with eastward drifting omega bands, *Journal of Geophysical Research*, *50*, 194–201, 1982.

Aubry, M., Russell, C., and Kivelson, M., Inward motion of the magnetopause before a substorm, *Journal of Geophysical Research*, *75*, 7018–7031, 1970.

Belian, R., Baker, D., Higbie, P., and Hones, E., High-resolution energetic particle measurements at 6.6 Re 2: High-energy proton drift echoes, *Journal of Geophysical Research*, *83*, 4857–4868, 1978.

Birmingham, T., The effects of pressure anisotropy on Birkeland currents in dipole and stretched magnetospheres, *Journal of Geophysical Research*, *97*, 3919–3927, 1992b.

Borovsky, J., Auroral arc thicknesses as predicted by various theories, *Journal of Geophysical Research*, *98*, 6101–6138, 1993.

Brekke, A., *Physics of the upper polar atmosphere*, Wiley-Praxis, 1997.

Brekke, A. and Egeland, A., *Nordlyset: kulturarv og vitenskap*, Grøndahl Dreyers Forlag AS, Oslo, 1994.

Burke, W., Silevitch, M., and Hardy, D., Observations of small-scale auroral vortices by the S3-2 satellite, *Journal of Geophysical Research*, *88*, 3127–3137, 1983.

Davies, J., Lester, M., Jenkins, B., and Moffett, R., Dayside frictional heating: EISCAT observations and comparison with model results, *Journal of Atmospheric and Terrestrial Physics*, *57*, 775–793, 1995.

Davis, T., Observed characteristics of auroral forms, *Space Science Reviews*, *22*, 77–113, 1978.

Davis, T. and Hallinan, T., Small-scale auroral arc distortions, *Planetary and Space Science*, *18*, 1735–1744, 1970.

Davis, T. and Hallinan, T., Auroral spirals, 1. Observations, *Journal of Geophysical Research*, *81*, 3953–3958, 1976.

del Pozo, C., Williams, P., Gazey, N., Smith, P., Honary, F., and Kosch, M., Multi-instrument observations of the dynamics of auroral arcs: A case study, *Journal of Atmospheric and Solar-Terrestrial Physics*, *64*, 1601–1616, 2002.

Dungey, J., Interplanetary magnetic field and the auroral zones, *Physical Review Letters*, *6*, 47–48, 1961.

Elphinstone, R. and Hearn, D., Mapping auroral distribution during quiet times and substorm recovery, in *Proceedings of the First International Conference on Substorms*, pp. 13–18, 1992.

Elphinstone, R., Murphee, J., and Cogger, L., What is a global auroral substorm?, *Reviews of Geophysics*, *34*, 169–232, 1996.

Evans, D., Precipitating electron fluxes formed by a magnetic field aligned potential difference, *Journal of Geophysical Research*, *79*, 2853–2858, 1974.

Giovanelli, R., Magnetic and electric phenomena in the Sun's atmosphere associated with sunspots, *Month. Not. Roy. Astr. Soc.*, *107*, 338, 1947.

Gonzales, W. and Tsurutani, B., Criteria of interplanetary parameters causing intense magnetic storms (Dst$\leq$-100nT), *Planetary and Space Science*, *35*, 1101–1109, 1987.

Greenwald, R., Weiss, W., and Nielsen, E., STARE: A new radar auroral backscatter experiment in northern Scandinavia, *Radio Science*, *13*, 1021–1039, 1978.

Hallinan, T., Auroral spirals, 2. Theory, *Journal of Geophysical Research*, *81*, 3959–3965, 1976.

Harang, L., The mean field of disturbance of polar geomagnetic storms, *Terrestrial Magnetism and Atmospheric Electricity*, *51*, 353, 1946.

Hedin, A., MSIS-86 thermospheric model, *Journal of Geophysical Research*, *92*, 4649–4662, 1987.

Hedin, A., Extension of the MSIS thermosphere model into the middle and lower atmosphere, *Journal of Geophysical Research*, *96*, 1159–1172, 1991.

Heppner, J., The Harang discontinuity in auroral belt ionospheric currents, *Geophysical Publications*, *29*, 105, 1972.

Heppner, J. and Maynard, N., Empirical high-latitude electric field model, *Journal of Geophysical Research*, *92*, 4467–4489, 1987.

Higbie, P., Belian, R., and Baker, D., High-resolution energetic particle measurements at 6.6 Re 1: Electron micropulsations, *Journal of Geophysical Research*, *83*, 4857–4855, 1978.

Hones, E., Baker, D., Bame, S., Feldman, W., Gosling, J., McComas, D., Zwickl, R., Slavin, J., Smith, E., and Tsurutani, B., Structure of the magnetotail at 220 Re, *Geophysical Research Letters*, *11*, 5–7, 1984.

Iijima, T. and Potemra, T., The amplitude distribution of field-aligned currents at northern high latitudes observed by Triad, *Journal of Geophysical Research*, *81*, 2165–2174, 1976a.

Iijima, T. and Potemra, T., Large-scale characteristics of field-aligned currents associated with substorms, *Journal of Geophysical Research*, *83*, 599–615, 1978.

Inhester, B., Untiedt, J., Segatz, M., and Kürschner, M., Direct determination of the local ionospheric Hall conductance distribution from two-dimensional electric and magnetic field data, *Journal of Geophysical Research*, *97*, 4073–4083, 1992.

Janhunen, P., Reconstruction of electron precipitation characteristics from a set of multi-wavelength digital all-sky auroral images, *Journal of Geophysical Research*, *106*, 18505–18516, 2001.

Janhunen, P. and Olsson, A., New model for auroral acceleration: O-shaped potential structure cooperating with waves, *Annales Geophysicae*, *18*, 596–607, 2000.

Janhunen, P. and Olsson, A., A hybrid simulation model for a stable auroral arc, *Annales Geophysicae*, *20*, 1603–1616, 2002.

Johnstone, A., The mechanism of pulsating aurora, *Annales Geophysicae*, *1*, 397–410, 1983.

Kallio, E., Pulkkinen, T., Koskinen, H., Viljanen, A., Slavin, J., and Ogilvie, K., Loading-unloading processes in the nightside ionosphere, *Geophysical Research Letters*, *27*, 1627–1630, 2000.

Kamide, Y., The auroral electrojets: Relative importance of ionospheric conductivities and electric fields, in *Auroral physics*, pp. 385–399, Cambridge University Press, 1991.

Kirkwood, S., SPECTRUM — A computer algorithm to derive the flux-energy spectrum of precipitating particles from EISCAT electron density profiles, *IRF Technical Report*, *034*, 1988.

Kirkwood, S. and Osepian, A., Quantitative studies of energetic particle precipitation using incoherent scatter radar, *Journal of Geomagnetism and Geoelectricity*, *47*, 783–799, 1995.

Knudsen, D., Donovan, E., Cogger, L., Jackel, B., and Shaw, W., Width and structure of mesoscale optical auroral arcs, *Geophysical Research Letters*, *28*, 705–708, 2001.

Koskinen, H., Pulkkinen, T., and Pellinen, R., Mapping of the auroral horn into the magnetotail, *Planetary and Space Science*, *38*, 1179–1186, 1990.

Koskinen, H., Lopez, R., Pellinen, R., Pulkkinen, T., Baker, D., and Bösinger, T., Pseudobreakup and substorm growth phase in the ionosphere and magnetosphere, *Journal of Geophysical Research*, *98*, 5801–5813, 1993.

Krall, N. and Trivelpiece, A., *Principles of Plasma Physics*, McGraw-Hill, New York, 1973.

Lanchester, B. and Rees, M., Field-aligned current reversals and fine structure in a dayside auroral arc, *Planetary and Space Science*, *35*, 759–768, 1987.

Lanchester, B., Rees, M., Lummerzheim, D., Otto, A., Frey, H., and Kaila, K., Large fluxes of auroral electrons in filaments of 100 m width, *Journal of Geophysical Research*, *102*, 9741–9748, 1997.

Lanchester, B., Rees, M., Lummerzheim, D., Otto, A., Sedgemore-Schulthess, K., Zhu, H., and McCrea, I., Ohmic heating as evidence for strong field-aligned currents in filamentary aurora, *Journal of Geophysical Research*, *106*, 1785–1794, 2002.

Liou, K., Meng, C.-I., Lui, A., Newell, P., and Wing, S., Magnetic dipolarization with substorm expansion onset, *Journal of Geophysical Research*, *107*, doi:10.1029/2001JA000179, 2002.

Mäkinen, S., *All-Sky Camera Calibration*, Master's thesis, Helsinki University of Technology, 2001.

Marklund, G., Karlsson, T., and Clemmons, J., On low-altitude particle acceleration and intense electric fields and their relationship to black aurora, *Journal of Geophysical Research*, *102*, 17509–17522, 1997.

McComas, D., Bame, S., Barker, P., Delapp, D., Feldman, W., Gosling, J., Santiago, E., Skoug, R., Tokar, R., Riley, P., Phillips, J., and Griffee, J., An unusual coronal mass ejection: First Solar Wind Electron, Proton, Alpha Monitor (SWEPAM) results from the Advanced Composition Explorer, *Geophysical Research Letters*, *25*, 4289–4292, 1998.

McPherron, R., Growth phase of magnetospheric substorms, *Journal of Geophysical Research*, *75*, 5592–5599, 1970.

McPherron, R., Physical processes producing magnetospheric substorms and magnetic storms, in *Geomagnetism*, vol. 4, pp. 593–739, Academic Press Limited, 1991.

McPherron, R., Russell, C., and Aubry, M., Satellite studies of magnetospheric substorms on August 15, 1968, *Journal of Geophysical Research*, *78*, 3131–3149, 1973.

Nakamura, R., Oguti, T., Yamamoto, T., and Kokubun, S., Equatorward and poleward expansion of the auroras during auroral substorms, *Journal of Geophysical Research*, *98*, 5743–5759, 1993.

Nakamura, R., Baker, D., Yamamoto, T., Belian, R., Bering, E., Benbrook, J., and Theal, J., Particle and field signatures during pseudobreakup and major expansion onset, *Journal of Geophysical Research*, *99*, 207–221, 1994.

Nielsen, E. and Schlegel, K., A first comparison of STARE and EISCAT electron drift velocity measurements, *Journal of Geophysical Research*, *88*, 5745–5750, 1983.

Nielsen, E. and Schlegel, K., Coherent radar Doppler measurements and their relationship to the ionospheric electron drift velocity, *Journal of Geophysical Research*, *90*, 3498–3504, 1985.

Nygrén, T., *Introduction to incoherent scatter measurements*, Invers Oy, 1994.

Oikarinen, L., Polarization of light in UV-visible limb radiance measurements, *Journal of Geophysical Research*, *106*, 1533–1544, 2001.

Opgenoorth, H., Pellinen, R., Baumjohann, W., Nielsen, E., Marklund, G., and Eliasson, L., Three-dimensional current flow and particle precipitation in a westward travelling surge (observed during the barium-GEOS rocket experiment), *Journal of Geophysical Research*, *88*, 3138–3152, 1983.

Opgenoorth, H., Persson, M., Pulkkinen, T., and Pellinen, R., Recovery phase of magnetospheric substorms and its association with morning-sector aurora, *Journal of Geophysical Research*, *99*, 4115–4129, 1994.

Priest, E. and Forbes, T., New models for fast steady state magnetic reconnection, *Journal of Geophysical Research*, *91*, 5579–5588, 1986.

Pulkkinen, T., Pseudobreakup or substorm?, in *Proceedings of the Third International Conference on Substorms*, pp. 285–293, 1996.

Pulkkinen, T., Koskinen, H., and Pellinen, R., Mapping of auroral arcs during substorm growth phase, *Journal of Geophysical Research*, *96*, 21087–21094, 1991.

Rees, M., Auroral ionization and excitation by incident energetic electrons, *Planetary and Space Science*, *11*, 1209–1218, 1963.

Rees, M., *Physics and Chemistry of the Upper Atmosphere*, Cambridge University Press, New York, 1989.

Rees, M. and Luckey, D., Auroral electron energy derived from ratio of spectroscopic emissions, 1, Model computations, *Journal of Geophysical Research*, *104*, 24565–24585, 1974.

Reeves, G., Fritz, T., Cayton, T., and Belian, R., Multi-satellite measurements of the substorm injection region, *Geophysical Research Letters*, *17*, 2015–2018, 1990.

Risbeth, H. and van Eyken, A., EISCAT: early history and the first ten years of operation, *Journal of Atmospheric and Terrestrial Physics*, *55*, 525–542, 1993.

Røyrvik, O., *Pulsating aurora: Local and global morphology*, Ph.D. thesis, University of Alaska, Fairbanks, 1976.

Sergeev, V., Tanskanen, P., Mursula, K., Korth, A., and Elphic, R., Current sheet thickness in the near-Earth plasma sheet during substorm growth phase, *Journal of Geophysical Research*, *95*, 3819–3828, 1990.

Sergienko, T. and Ivanov, V., A new approach to calculate the excitation of atmospheric gases by auroral electron impact, *Annales Geophysicae*, *11*, 717–727, 1993.

Smith, C., Acuna, M., Burlaga, L., Heureux, J., Ness, N., and Scheifele, J., The ACE Magnetic Field Experiment, *Space Science Reviews*, *86*, 613–632, 1998.

Syrjäsuo, M., *FMI All-Sky Cameras*, no. 25 in Geophysical Publications, Finnish Meteorological Institute, 2001.

Torr, M., Torr, D., Zukic, M., Johnson, R., Ajello, J., Banks, P., Clark, K., Cole, K., Keffer, C., Parks, G., Tsurutani, B., and Spann, J., A far ultraviolet imager for the international solar-terrestrial physics mission, *Space Science Reviews*, *71*, 329–383, 1995.

Trondsen, T. and Cogger, L., A survey of small-scale spatially periodic distortions of auroral forms, *Journal of Geophysical Research*, *103*, 9405–9415, 1998.

Uspensky, M., Koustov, A., Janhunen, P., Pellinen, R., Danskin, D., and Nozawa, S., STARE velocities: the importance of off-orthogonality and ion motion, *Annales Geophysicae*, *21*, 729–744, 2003.

Voronkov, I., Donovan, E., Jackel, B., and Samson, J., Large-scale vortex dynamics in the evening and midnight auroral zone: Observations and simulations, *Journal of Geophysical Research*, *105*, 18505–18518, 2000.

Yumoto, K., Takahashi, K., Saito, T., Menk, F., Fraser, B., Potemra, T., and Zanetti, L., Some aspects of the relation between Pi 1-2 magnetic pulsations observed at L=1.3–2.1 on the ground and substorm-associated magnetic field variations in the near-Earth magnetotail observed by AMPTE CCE, *Journal of Geophysical Research*, *94*, 3611–3618, 1989.